Reversible methylation of m6Am in the 5' cap controls mRNA stability

Jan Mauer, Xiaobing Luo, Alexandre Blanjoie, Xinfu Jiao, Anya V Grozhik, Deepak P Patil, Bastian Linder, Brian F Pickering, Jean-Jacques Vasseur, Qiuying Chen, et al.

To cite this version:

Jan Mauer, Xiaobing Luo, Alexandre Blanjoie, Xinfu Jiao, Anya V Grozhik, et al.. Reversible methylation of m6Am in the 5' cap controls mRNA stability. Nature, 2017, 541 (7637), pp.371-375. 10.1038/nature21022 . hal-02197215

HAL Id: hal-02197215
https://hal.science/hal-02197215

Submitted on 31 Jan 2024

Published in final edited form as:

Nature. 2017 January 19; 541(7637): 371–375. doi:10.1038/nature21022.

Reversible methylation of m^6A_m in the 5′ cap controls mRNA stability

Jan Mauer[1], **Xiaobing Luo**[2], **Alexandre Blanjoie**[3], **Xinfu Jiao**[2], **Anya V. Grozhik**[1], **Deepak P. Patil**[1], **Bastian Linder**[1], **Brian F. Pickering**[1], **Jean-Jacques Vasseur**[3], **Qiuying Chen**[1], **Steven S. Gross**[1], **Olivier Elemento**[4,5], **Françoise Debart**[3], **Megerditch Kiledjian**[2], and **Samie R. Jaffrey**[1]

[1]Department of Pharmacology, Weill Cornell Medicine, Cornell University, New York, New York 10065, USA

[2]Department of Cell Biology and Neuroscience, Rutgers University, Piscataway, New Jersey 08854, USA

[3]Department of Chemistry, IBMM UMR 5247, CNRS, Université de Montpellier ENSCM, UM Campus Triolet, Place E. Bataillon, 34095 Montpellier Cedex 05, France

[4]Department of Physiology and Biophysics, Weill Cornell Medicine, Cornell University, New York, New York 10065, USA

[5]HRH Prince Alwaleed Bin Talal Bin Abdulaziz Alsaud Institute for Computational Biomedicine, Weill Medical College, Cornell University, New York, New York 10065, USA

Abstract

Internal bases in mRNA can be subjected to modifications that influence the fate of mRNA in cells. One of the most prevalent modified bases is found at the 5′ end of mRNA, at the first encoded nucleotide adjacent to the 7-methylguanosine cap. Here we show that this nucleotide, N^6,2′-*O*-dimethyladenosine (m^6A_m), is a reversible modification that influences cellular mRNA fate. Using a transcriptome-wide map of m^6A_m we find that m^6A_m-initiated transcripts are markedly more stable than mRNAs that begin with other nucleotides. We show that the enhanced stability of m^6A_m-initiated transcripts is due to resistance to the mRNA-decapping enzyme DCP2. Moreover, we find that m^6A_m is selectively demethylated by fat mass and obesity-associated protein (FTO). FTO preferentially demethylates m^6A_m rather than N^6-methyladenosine (m^6A), and reduces the stability of m^6A_m mRNAs. Together, these findings show that the methylation

---

Reprints and permissions information is available at www.nature.com/reprints.

Correspondence and requests for materials should be addressed to S.R.J. (srj2003@med.cornell.edu).

Supplementary Information is available in the online version of the paper.

Author Contributions S.R.J., M.K., J.M. and X.J. designed the experiments. J.M., X.L., X.J. and A.V.G. carried out the experiments. D.P.P. carried out the analysis of covariance. B.L. and B.F.P. analysed the previously published ribosome profiling datasets. F.D., J.V. and A.B. synthesized modified oligonucleotides. S.S.G. and Q.C. carried out mass spectrometry analysis. O.E. performed analysis on *Fto* knockout MeRIP-seq datasets. S.R.J. and J.M. wrote the manuscript with input from all authors.

The authors declare no competing financial interests.

Readers are welcome to comment on the online version of the paper.

Reviewer Information *Nature* thanks O. Namy and the other anonymous reviewer(s) for their contribution to the peer review of this work.

status of m^6A_m in the 5′ cap is a dynamic and reversible epitranscriptomic modification that determines mRNA stability.

An emerging concept in gene expression regulation is that a diverse set of modified nucleotides is found internally within mRNA, and these modifications constitute an epitranscriptomic code. The initial concept of the epitranscriptome was introduced with the transcriptome-wide mapping of N^6-methyladenosine (m^6A), which revealed that m^6A is found in at least a fourth of all mRNAs, typically near stop codons[1,2]. Notably, adenosine methylation to form m^6A may be reversible. FTO and AlkB family member 5 (ALKBH5) both show demethylation activity towards RNA containing m^6A (refs 3,4). Thus, the epitranscriptome may be highly dynamic and subject to reversible base modifications that influence mRNA function.

In addition to internal base modifications, the 5′ end of mRNAs contains methyl modifications that are thought to be constitutive. mRNA biogenesis involves the addition of an N^7-methylguanosine (m^7G) cap with a triphosphate linker to the 5′ end of mRNAs. mRNAs are also methylated at the 2′-hydroxyl position of the ribose sugar of the first, and sometimes the second, nucleotide adjacent to the m^7G cap[5,6]. These modifications recruit translation initiation factors to mRNA and allow the cell to discriminate host from viral mRNA[7].

Although the extended 5′ cap structure contains these fixed methyl modifications, early studies by Moss and colleagues showed that one additional methyl modification can be detected in up to 30% of mRNA caps[8]. If the first nucleotide following the m^7G cap is 2′-*O*-methyladenosine (A_m), it can be further methylated at the N^6-position by an unidentified nucleocytoplasmic methyltransferase[9] to form N^6,2′-*O*-dimethyladenosine (m^6A_m) (Fig. 1a)[8]. Since 2′-*O*-methylation is essentially always detected at the first nucleotide, mRNAs can have either A_m or m^6A_m as the first nucleotide, but not A or m^6A (ref. 10). The function of m^6A_m is unknown.

Here we show that the extended mRNA cap carries dynamic and reversible epitranscriptomic information. We find that m^6A_m in its physiological context adjacent to the m^7G cap can be readily converted to A_m by FTO *in vitro* and *in vivo*. Furthermore, we demonstrate that m^6A_m, and not m^6A, is the preferred cellular substrate for FTO. Using our transcriptome-wide map of m^6A_m, we find that m^6A_m transcripts are markedly more stable than mRNAs beginning with A_m or other nucleotides. Manipulation of m^6A_m levels by FTO depletion or FTO overexpression results in selective control of the abundance of m^6A_m-containing mRNAs in cells. We find that m^6A_m transcript stability is in part due to resistance to the mRNA-decapping enzyme DCP2. The significance of m^6A_m-mediated mRNA stabilization can be seen by examining DCP2-dependent mRNA degradation processes in cells, such as the pattern of mRNA degradation induced by microRNAs. These findings show that the cap-associated modified nucleotide m^6A_m is a dynamic and reversible epitranscrip-tomic modification that confers stability to mRNA in mammalian cells.

FTO targets methyladenine at transcription start sites

FTO exhibits demethylation activity towards m^6A in assays performed *in vitro*[4]. However, we previously observed that most m^6A residues are unaffected in FTO-deficient mice[11]. Only a few m^6A residues showed increased abundance based on our transcriptome-wide mapping using antibodies directed against N^6-methyladenine (6mA)[11]. To understand this selectivity, we asked if FTO demethylates m^6A residues based on their position within mRNAs. We measured the change in m^6A stoichiometry for each m^6A peak mapped in the *Fto*-knockout relative to the wild-type transcriptome. We used a previously described stoichiometry measurement in which the number of m^6A-containing RNA fragments at each peak is normalized to transcript abundance[1]. Notably, the m^6A stoichiometry in the *Fto*-knockout transcriptome was increased for m^6A residues closer to the 5′ end of the transcript (Extended Data Fig. 1a).

We recently showed that the antibodies used in these early m^6A mapping studies bind both m^6A and m^6A_m (ref. 12). These two nucleotides are found in mRNA and both contain the 6mA base[8]. As a result, early transcriptome-wide mapping studies of m^6A also contain misannotated peaks that are instead derived from m^6A_m (ref. 12).

The distribution of FTO-regulated peaks in the 5′ untranslated region (UTR) is reminiscent of transcription start sites in mRNA (Extended Data Fig. 1a), which are often marked by m^6A_m (ref. 12). Our recent single-nucleotide-resolution map of m^6A_m showed that m^6A_m and transcription start sites overlap in mRNA[12]. This pattern of transcription start sites occurs because many mRNAs can be initiated at multiple positions downstream of the annotated start site. Thus, we hypothesized that the FTO-regulated peaks reflect m^6A_m rather than m^6A.

FTO demethylates m^6A_m in an m^7G cap-dependent manner

To determine whether FTO can target m^6A_m we measured FTO-mediated demethylation of a 21-nucleotide-long RNA with a 5′ m^7G cap followed by m^6A_m. FTO treatment readily converted m^6A_m to A_m, indicating demethylation at the N^6-position (Fig. 1b, Extended Data Fig. 1b). Next, we added FTO (100 nM) to an equimolar mixture of the m^6A_m RNA and an RNA containing m^6A in its physiological consensus. FTO demethylated nearly all m^6A_m in 60 minutes, while m^6A demethylation was not readily detected (Fig. 1c).

Demethylation of m^6A was only readily detected using higher concentrations of FTO (200 nM), consistent with previous reports which used a 5:1 ratio of substrate and enzyme[4]. However, demethylation of m^6A_m was achieved with substantially less FTO (20 nM) (Fig. 1d, Extended Data Figs 1c-g). The reported k_{cat} of FTO towards m^6A is relatively low compared to related dioxygenases (Extended Data Table 1). However, the k_{cat} for FTO towards m^6A_m is at least 20 times higher and the catalytic efficiency (k_{cat}/K_m) of FTO is approximately 100-fold higher towards m^6A_m than m^6A (Fig. 1d, Extended Data Table 1).

The activity of FTO towards m^6A_m was dependent on specific structural elements of the extended m^7G cap. FTO-mediated demethylation of m^6A_m was impaired when m^7G was substituted for G, and further reduction was seen when m^7G was removed altogether

(Extended Data Fig. 2a, b). Demethylation was further reduced when the triphosphate was shortened to a monophosphate. Notably, the 2′-*O*-methyl substi-tuent, which distinguishes m^6A_m from m^6A, was also important for the demethylation activity of FTO. By contrast, FTO-mediated demethylation of m^6A was poor in diverse sequence contexts (Extended Data Fig. 2a, b).

Mass spectrometry confirmed FTO-mediated demethylation of m^6A_m to A_m (Extended Data Fig. 2c, d). However, in addition to A_m, *N*6-hydroxymethyl,2′-*O*-methyladenosine (hm^6A_m) was also detected. Previous analysis of FTO activity towards m^6A showed that FTO-mediated demethylation occurs via a hydroxymethylated intermediate[13]. Therefore, FTO-mediated demethylation of m^6A_m may create additional cap diversity comprising oxidized 5′ caps.

FTO controls the balance between m^6A_m and A_m *in vivo*

We next asked whether FTO demethylates m^6A_m in cellular mRNA. To quantify the ratio of m^6A_m to A_m in mRNA, we used thin-layer chromatography (TLC)[14]. The m^7G cap was enzymatically removed from mRNA and the exposed 5′ nucleotide was radiolabeled with [γ-^{32}P]-ATP. Two-dimensional TLC of the nucleotide hydrolysate reveals the identity of the 5′ nucleotide (Extended Data Fig. 3a)[14]. Treatment of cellular mRNA with recombinant FTO resulted in an approximately 80% reduction of the m^6A_m:A_m ratio (Fig. 2a). Notably, the same mRNA samples did not show decreased m^6A upon FTO treatment (Extended Data Fig. 3b). These results suggest that FTO does not efficiently demethylate m^6A in mRNA.

To determine whether FTO demethylates m^6A_m in cells, we transfected HEK293T cells with Flag-FTO. This resulted in a significantly reduced m^6A_m:A_m ratio relative to control cells (Fig. 2b). Although FTO is primarily nuclear, hypothalamic neurons exhibit cytosolic FTO after food deprivation[15]. Since there is no reported approach to efficiently induce cytosolic localization of FTO in cultured cells, we expressed FTO containing a nuclear-export signal (NES–FTO) in HEK293T cells (Extended Data Fig. 3c, d). This resulted in a more pronounced drop in the m^6A_m:A_m ratio than wild-type FTO expression (Extended Data Fig. 3e). At this expression level, NES–FTO did not reduce m^6A levels (Extended Data Fig. 3f). Thus, FTO demethylates m^6A_m in cells and cytosolic translocation of FTO may further enhance the demethylation of cytoplasmic m^6A_m mRNAs.

FTO knockdown further increased the already high[14] m^6A_m:A_m ratio in cells (Fig. 2c). Similarly, the m^6A_m:A_m ratio was increased in *Fto*-knockout mouse embryos compared to wild type (Extended Data Fig. 3g). No increase in m^6A levels was detectable in *FTO*-knockdown cells or *Fto*-knockout mouse embryos (Extended Data Figs 3h, i). By contrast, *ALKBH5* knockdown increased m^6A levels without increasing m^6A_m levels and ALKBH5 expression selectively demethylated m^6A but not m^6A_m (Extended Data Figs 4a–d). These results suggest that FTO targets m^6A_m whereas ALKBH5 targets m^6A *in vivo*.

m^6A_m mRNAs exhibit increased half-life in cells

To determine whether m^6A_m confers unique effects on mRNA, we first classified cellular mRNAs based on whether they begin with m^6A_m, A_m, 2′-*O*-methylcytidine (C_m), 2′-*O*-

methylguanosine (G_m) or 2′-*O*-methyluridine (U_m). mRNAs beginning with m^6A_m were identified by miCLIP[12] (Supplementary Table 1). miCLIP-mapped m^6A_m residues were validated based on their overlap with transcription start sites and their preferential localization in a sequence context matching the core initiator motif[16] (Extended Data Fig. 5a, b, Supplementary Table 1). mRNAs that did not contain m^6A_m were considered to begin with A_m, C_m, G_m or U_m based on the annotated starting nucleotide (Supplementary Table 2).

We next asked whether mRNA stability is linked to the identity of the first nucleotide. mRNAs beginning with A_m, C_m, G_m and U_m exhibited a very similar distribution of half-lives, with an average of around 6 h in HEK293T cells (Fig. 3a). However, mRNAs that begin with an m^6A_m were markedly more stable, with an average increase in half-life of approximately 2.5 h (Fig. 3a, Extended Data Fig. 5c–e, Supplementary Table 3). A link between m^6A_m and mRNA stability is also seen when examining the distribution of m^6A and m^6A_m miCLIP reads in long-lived and short-lived mRNAs (Extended Data Fig. 5f, g).

We reasoned that if m^6A_m stabilizes mRNA, then this would lead to increased m^6A_m mRNA levels. Indeed, m^6A_m mRNAs exhibit higher transcript levels than mRNAs that begin with A_m, C_m, G_m or U_m (Fig. 3b). Although the increased expression levels could be influenced by transcription rates, the half-life data suggests that increased mRNA stability contributes to the increased abundance of m^6A_m mRNAs. Taken together, these data indicate that the first nucleotide is an important determinant of mRNA stability and abundance.

Additionally, m^6A_m mRNAs may increase translation efficiency (Extended Data Figs 6a-f). This is in line with a previous study that observed increased translation efficiency of mRNAs containing methylated adenine at the transcription start site[17].

Alterations in m^6A_m levels control mRNA stability

To test directly whether m^6A_m can confer stability to mRNA, we synthe sized polyadenylated mRNAs starting with either m^7GpppA_m or $m^7Gpppm^6A_m$ *in vitro*. Electroporation of these mRNAs into HEK293T cells showed that the m^6A_m mRNA was more stable than the A_m-initiated mRNA (Extended Data Fig. 7a).

Next, we selectively reduced cellular m^6A_m levels by expressing NES–FTO and monitored mRNA half-life. At the level of transfection used, changes in m^6A were not detectable, but m^6A_m levels were significantly reduced (Extended Data Fig. 3c–f). Analysis of transcriptome-wide fold-changes in mRNA half-lives showed that NES–FTO expression causes a significant decrease in m^6A_m mRNA half-life compared to mRNAs initiated with A_m (Fig. 3c). m^6A-containing mRNAs were unaffected (Extended Data Fig. 7b). The effect of NES–FTO on m^6A_m mRNAs was also seen when monitoring the stability of individual transcripts using BrU pulse–chase labelling (Extended Data Fig. 7c). These results suggest that demethy-lation of m^6A_m reduces the stability of mRNAs that begin with this nucleotide.

Although m^6A_m levels are typically high in most cell types[8,14], we further increased m^6A_m levels by *FTO* knockdown and measured mRNA levels using RNA-seq. Notably, mRNAs that start with m^6A_m showed higher abundance after *FTO* knockdown compared to A_m-initiated mRNAs (Fig. 3d). This effect was also seen in *Fto*-knockout mouse liver compared to wild type (Extended Data Fig. 7d). Notably, *ALKBH5* knockdown did not affect m^6A_m mRNAs (Extended Data Fig. 7e). We therefore conclude that increasing m^6A_m levels enhances the stability of these mRNAs.

m^6A_m confers reduced susceptibility to decapping

Since mRNA degradation often involves decapping, we considered the possibility that m^6A_m affects this process. Studies of the mRNA-decap-ping enzyme DCP2[18] have previously used RNAs with an m^7G cap, but did not examine the effect of the methylation state of the subsequent nucleotide. We generated m^7G-capped RNAs (m^7GpppRNA) with a ^{32}P-labelled γ-phosphate proximal to the m^7G. DCP2-mediated decapping releases radiolabelled m^7GDP, which was detected by TLC (Fig. 4a, Extended Data Fig. 8a). RNAs containing an m^7G cap followed by an unmodified adenosine or A_m showed equivalent efficiencies of decapping, indicating that the 2′-*O*-methyl modification does not affect DCP2-mediated decapping (Fig. 4b). However, RNAs with m^7G followed by m^6A_m or m^6A showed significantly reduced decapping (Fig. 4b, Extended Data Fig. 8b).

We next asked whether m^6A_m impairs decapping in cells. We reasoned that DCP2 deficiency would lead to increased A_m, C_m, G_m and U_m mRNA levels relative to m^6A_m mRNAs. Transcriptome-wide analysis showed increased levels of mRNAs that start with A_m, C_m, G_m or U_m in *DCP2*-deficient HEK293T cells compared to controls (Fig. 4c). m^6A_m mRNAs were less affected, indicating that they are less susceptible to DCP2-dependent degradation (Fig. 4c). As an additional control, we monitored the stability of individual mRNAs using BrU pulse–chase labelling. Notably, A_m mRNAs showed stabilization upon DCP2 depletion, while m^6A_m mRNAs were not significantly stabilized (Extended Data Fig. 8c). These results suggest that m^6A_m confers resistance to DCP2, resulting in increased mRNA stability.

m^6A_m impairs microRNA-mediated mRNA degradation

One unresolved question in microRNA-mediated degradation is why some mRNAs are efficiently degraded by microRNAs while others show less robust degradation[19]. MicroRNA-mediated mRNA degradation involves decapping[20]. We therefore asked whether microRNA-mediated degradation could be influenced by the presence of m^6A_m.

To test this, we examined gene expression data sets of HEK293 cells deficient in DICER and AGO2[21]. In both cases, microRNA-mediated mRNA degradation is impaired, resulting in increased levels of microRNA-targeted mRNAs. If m^6A_m mRNAs were less susceptible to microRNA-mediated degradation, they would exhibit less-pronounced upregulation upon loss of DICER or AGO2. Indeed, mRNAs starting with A_m, C_m, G_m or U_m exhibited a significantly higher increase in expression than m^6A_m mRNAs (Fig. 4d, Extended Data Fig. 8d-f). Thus, m^6A_m mRNAs are less susceptible to microRNA-mediated degradation.

Next, we asked whether m^6A_m mRNAs show reduced susceptibility to microRNA-mediated mRNA degradation upon introduction of a single microRNA. We therefore analysed gene expression data sets from miR-155-transfected HeLa cells[22] and mRNAs with predicted miR-155-binding sites. This analysis revealed that m^6A_m mRNAs were significantly more resistant to miR-155-mediated mRNA degradation compared to other mRNAs (Extended

Data Figs 8g, h). These data suggest that m^6A_m reduces the susceptibility of mRNAs to endogenous decay pathways such as microRNA-mediated mRNA degradation.

Discussion

Here we identify m^6A_m as a dynamic and reversible epitranscriptomic mark. In contrast to the concept that epitranscriptomic modifications are found internally in mRNA, we find that the 5′ cap harbours epitranscriptomic information that determines the fate of mRNA. The presence of m^6A_m in the extended cap confers increased mRNA stability, while A_m is associated with baseline stability. m^6A_m has long been known to be a pervasive modification in a large fraction of mRNA caps in the transcriptome[8], making it the second most prevalent modified nucleotide in cellular mRNA. Dynamic control of m^6A_m can therefore influence a large portion of the transcriptome.

The concept of reversible base modifications is appealing since it raises the possibility that the fate of an mRNA can be determined by switching a modification on and off. Our data show that FTO is an m^6A_m ‘eraser’ and forms A_m in cells. FTO resides in the nucleus, where it probably demethylates nuclear RNA and newly synthesized mRNAs. Demethylation of cytoplasmic m^6A_m mRNAs may be induced by stimuli that induce cytosolic translocation of FTO.

The specificity of FTO towards m^6A_m in cells is supported by the finding that depletion of FTO increases m^6A_m mRNA levels relative to A_m mRNAs, while m^6A-containing mRNAs are largely unaffected. Although FTO prefers m^6A_m, high levels of FTO overexpression cause small but measurable reductions in m^6A levels in specific mRNAs[23]. Additionally, an earlier study reported small increases in total m^6A levels in cell lines following *FTO* knockdown[4]. m^6A measurement in FTO-depleted cells is complicated by the fact that FTO depletion causes increases in m^6A_m mRNA expression levels, which can lead to indirect changes in m^6A levels. Higher mRNA expression also results in increased m^6A peak calling owing to the stochastic nature of detecting m^6A modifications in low-abundance mRNAs[24].

Prior to our recent development of single-nucleotide-resolution m^6A and m^6A_m mapping techniques[12], m^6A mapping inadvertently included m^6A_m sites that were misannotated as m^6A. These older techniques should more accurately be designated as 6mA mapping (that is, the methylated base) to reflect their inability to distinguish m^6A_m and m^6A. Similarly, m^6A immunoblot and m^6A-IP qRT-PCR cannot distinguish between m^6A and m^6A_m. We find that the upregulated peaks in the *Fto*-knockout transcriptome[11], which are enriched in the 5′ UTR, probably reflect FTO-regulated m^6A_m sites. A similar increase in 5′ UTR peaks was reported in a m^6A mapping study of *Fto*-deficient mouse fibroblasts[25]. The 5′ UTR enrichment of these peaks suggests that these residues may also reflect m^6A_m.

Previous studies on FTO should be reconsidered in light of its preferential activity towards m^6A_m. FTO has been linked to altered splicing of mRNAs, which may indicate a role for m^6A_m in this process[26]. *FTO* knockdown increases the translation of *HSPA1A*[23,25]. Although site-directed mutagenesis supports a role for 5′ UTR m^6A in the translation of this mRNA[25], m^6A_m also probably contributes to this effect owing to its sensitivity to FTO.

FTO-deficient mice display diverse phenotypes ranging from growth retardation to metabolic changes and abnormalities in brain reward pathways[11,27]. Humans with *FTO* loss-of-function mutations exhibit growth retardation and malformations[28]. Since m^6A_m mRNAs are enriched in functional categories linked to RNA splicing, translation and metabolism (Extended Data Fig. 9), alterations in these pathways may contribute to the physiological effects of FTO deficiency.

DCP2 is a ‘reader’ of the mRNA cap modification state, thereby contributing to the stability of m^6A_m mRNAs. m^6A_m impairs mRNA decapping, rendering m^6A_m mRNAs less susceptible to microRNA-mediated mRNA degradation. Therefore, m^6A_m probably contributes to the poorly understood variability in mRNA responses to microRNAs seen in cells[29].

The effects of m^6A_m contrast with those of m^6A. While m^6A_m exhibits a stabilizing effect, m^6A is associated with enhanced mRNA degradation (ref. 30). However, both m^6A_m and m^6A residues in the 5′ UTR are linked to increased translation[23], suggesting that these different methylated forms of adenosine in the 5′ UTR enhance translation initiation. Thus, the location of the modified nucleotide and the specific combination of methyl groups on adenosine residues encode distinct functional consequences on the mRNA.

Online Content

Methods, along with any additional Extended Data display items and Source Data, are available in the online version of the paper; references unique to these sections appear only in the online paper.

Methods

No statistical methods were used to predetermine sample size. The experiments were not randomized and the investigators were not blinded to allocation during experiments and outcome assessment.

Synthesis and characterization of synthetic oligonucleotides

The sequences of all the oligonucleotides used in this study are shown in Supplementary Table 4. The oligonucleotide containing an internal N^6-methyladenosine (m^6A) in a DRACH context was synthesized by TriLink BioTechnologies.

All other synthetic RNA oligonucleotides were chemically assembled on an ABI 394 DNA synthesizer (Applied Biosystems) from commercially available long-chain alkylamine controlled-pore glass (LCAA-CPG) solid support with a pore size of 1,000 Å derivatized through the succinyl linker with 5′-*O*-dimethoxytrityl-2′-*O*-Ac-uridine (Link Technologies). All RNA sequences were prepared using phosphoramidite chemistry at 1 μmol scale in Twist oligonucleotide synthesis columns (Glen Research) from commercially available 2′-*O*-pivaloyloxymethyl amidites (5′-*O*-DMTr-2′-*O*-PivOM-[U, C^{Ac}, A^{Pac} or G^{Pac}]-3′-*O*-(*O*-cyanoethyl-*N,N*-diisopropylphosphoramidite)[31] (Chemgenes). The 5′ terminal adenosine can be unmodified A, or methylated in 2′-OH (A_m), or in N^6 position (m^6A) or in both positions (m^6A_m). The 5′-*O*-DMTr-2′-*O*-Me-A^{Pac}-3′-*O*-(*O*-cyanoethyl-*N,N*-diisopropylphosphoramidite) (Chemgenes) was used to introduce A_m at the 5′-end of RNA. For the production of m^6A-RNAs or m^6A_m-RNAs, the preparation of m^6A and m^6A_m phosphoramidite building blocks was performed by a selective one-step methylation of the commercially available 2′-*O*-PivOM-Pac-A-CE phosphoramidite or 2′-*O*-Me-Pac-A-CE phosphoramidite, respectively. All oligoribonucleotides were synthesized using standard protocols for solid-phase RNA synthesis with the PivOM methodology[32].

After RNA assembly, the 5′-hydroxyl group of the 5′-terminal adenosine (A): A, A_m, m^6A or m^6A_m of RNA sequences, still anchored to solid support, was phosphorylated and the resulting *H*-phosphonate derivative was oxidized and activated into a phosphoroimidazolidate derivative to react with either pyrophosphate (for ppp(A)-RNA synthesis)[33] or guanosine diphosphate (for Gppp(A)-RNA synthesis)[34]. To obtain the monophosphate of m^6A_m-RNA (pm^6A_m-RNA), the 5′-*H*-phosphonate RNA was treated with a mixture of *N,O*-bis-trimethylacetamide and triethylamine in acetonitrile, and then oxidized with a *tert*-butyl hydroperoxide solution[35].

After deprotection and release from the solid support upon basic conditions (DBU then aqueous ammonia treatment for 4 h at 37 °C), all RNA sequences were purified by IEX-HPLC[36], they were obtained with high purity (>95%) and they were unambiguously characterized by MALDI-TOF spectrometry (Supplementary Table 4).

N^7 methylation of the purified Gppp(A)-RNAs to give m^7Gppp(A)-RNAs was carried out quantitatively using human mRNA guanine-N^7-methyltransferase and *S*-adenosylmethionine as previously described[34].

Measurement of enzymatic properties of FTO *in vitro*

Demethylation measurements were performed essentially as described previously[4], with the exception that all reactions were carried out at 37 °C. The demethylation activity assay was performed in 20-50 μl of reaction mixture containing the indicated quantities of synthetic RNA oligonucleotide or mRNA, the indicated quantities of FTO, 75 mM of $(NH_4)2Fe(SO_4)2$, 300 mM α-ketoglutarate, 2 mM sodium L-ascorbate, 150 mM KCl and 50 mM HEPES buffer, pH 7.0. The reaction was incubated at 37 °C for the indicated times, quenched by the addition of 1 mM of EDTA followed by inactiva-tion of the enzymes for 5 min at 95 °C.

Sample preparation for HPLC analysis

After demethylation by FTO, oligonucleotides were decapped with 25 units of RppH (NEB) in ThermoPol buffer for 2 h at 37 °C. RNA was subsequently digested to single nucleotides with 180 units of S1 nuclease (Takara) for 1 h at 37 °C. 5′ phosphates were removed with 5 units of rSAP (NEB) for 1 h at 37 °C. Before loading the samples onto the HPLC column, proteins were removed by size-exclusion chromatography with a 10 kDa cut-off filter (VWR).

HPLC analysis of demethylation activity

The HPLC analysis of nucleosides was performed on an Agilent 1100 system (Agilent Technologies). Separation was performed on a Poroshell 120 EC-C18 column (4μm, 150 × 4.6 mm, Agilent Technologies) equipped with an EC-C18 Guard cartridge (Agilent Technologies) at 22 °C. The mobile phase consisted of buffer A (25 mM NaH_2PO_4) and buffer B (100% acetonitrile). Pump control and peak integration was achieved using the ChemStation software (Rev. A.10.02, build 1757, Agilent Technologies). Samples were analysed at 2 ml min^{-1} flow rate with the following buffer A/B gradient: 7.5 min 95%/5%, 0.5 min 90%/10%, 2 min 10%/90%, 1 min 95%/5%. Retention times of the individual nucleosides was determined with synthetic standards (3.2 min for adenosine (A), 5.8 min for 2′-*O*-methyladenosine (A_m), 5.9 min for N^6-methyladenosine (m^6A), 7.9 min for N^6,2′-*O*-dimethyladenosine (m^6A_m). Guanosine was used as an internal control. After normalization of each peak area to the area of the guanosine peak area, the relative and absolute amount of individual nucleotides in each sample was determined based on the sequence of the input oligonucleotide.

Sample preparation for mass spectrometry

m^6A_m demethylation intermediates were generated essentially as described previously[13], with the difference that all reactions were carried out at 37 °C. Capped oligonucleotides were incubated with 100 nM FTO for 10 min at 37 °C followed by digestion with 2 units of P1 nuclease for an additional 15 min. Notably, P1 nuclease does not cleave the triphosphate linker of the cap and thus specifically releases the $m^7Gpppm^6A_m$ dinucleotide, while digesting the RNA backbone down to single nucleotides. To preserve the unstable demethylation intermediates[13], the nucleotide mixture was immediately frozen in liquid nitrogen until further analysis.

Detection of demethylation intermediates by mass spectrometry

FTO reaction products were extracted by cold 80% methanol:H_2O at 1:20 volume ratio. After removal of precipitated protein, 4 μl of supernatant was injected into LC/MS for accurate mass measurement of demethylation intermediates. The LC/MS-MS system comprised an Agilent Model 1260 Bio-inert infinity liquid chromatography system coupled to an Agilent iFunnel 6550 quadrupole time-of-flight mass spectrometer. Chromatography of the reaction products was performed using aqueous normal phase (ANP) gradient separation, on Cogent Diamond Hydride (ANP) column (2.1 × 150 mm, 3.5 μm particle size; Microsolv Technology Corp). A precolumn filter (0.5 μm, Microsolv) was placed in front of the ANP column, to prevent column clogging. Mobile phases consisted of: (A) 50% isopropanol, containing 0.025% acetic acid; and (B) 90% acetonitrile containing 5 mM ammonium acetate. To eliminate the interference of metal ions on the chromatographic peak integrity and electrospray ionization, EDTA was added to the mobile phase at a final concentration of 6 μM. The following gradient was applied: 0-1.0 min, 99% B; 1.0-15.0 min, to 20% B; 15.0–29.0 min, 0% B; 29.1-37 min, 99% B. To minimize potential salt and other contaminants in the ESI source, a time segment was set to direct the first 0.5 min of column elute to waste.

Negative ion mass spectra in both profile and centroid mode were acquired in 2 GHz (extended dynamic range) mode, scanned at 1 spectrum per second over a mass/charge range of 20–1,000 Daltons. The QTOF capillary voltage was set 3,500 V and the fragmentor was set to 140 V. The nebulizer pressure was 35 p.s.i. and the nitrogen drying gas was 200 °C, delivered at a flow rate of 14 l min^{-1}. The sheath gas temperature was at 350 °C with sheath gas flow of 11 l min^{-1}. Raw data was analysed with Agilent MassHunter Qualitative Analysis software (version B6.0). Profile data was used to provide measured mass.

Cell culture and animals

HEK 293T/17 (ATCC CRL-11268; passage number 3-10; no further verification of cell line identity was performed) cells were maintained in DMEM (11995-065, ThermoFisher Scientific) with 10% FBS and antibiotics (100 units ml^{-1} penicillin and 100μg ml^{-11} of streptomycin) under standard tissue culture conditions. Cells were split using TrypLE Express (Life Technologies) according to the manufacturer's instructions. Mycoplasma contamination in cells were routinely tested by Hoechst staining. To obtain embryonic day (E) 14 *Fto*-knockout mouse embryos and livers, *Fto*-knockout mice were bred as previously described[27]. Only male animals were used in the current study. All experiments involving mice were approved by the Institutional Animal Care and Use Committee at Weill Cornell Medical College.

Antibodies

Antibodies used for western blot analysis or immunostaining were as follows: rabbit anti-DDDDK/Flag (ab1162, Abcam), rabbit anti-FTO (ab124892, Abcam), rabbit anti-GAPDH (ab9485, Abcam), mouse anti-ALKBH5 (ab69325, Abcam), mouse (β-actin (A2228, Sigma) and goat anti-rabbit IgG Alexa Fluor 546 (A11035, ThermoFisher Scientific). For m^6A individual-nucleotide-resolution cross-linking and immunoprecipitation (miCLIP), rabbit anti-m^6A (ab151230, Abcam) was used. An in-house-generated rabbit anti-DCP2 serum was used for detection of DCP2.

Knockdown and overexpression studies in HEK293T cells

FTO and *ALKBH5* knockdown experiments were carried out in HEK293T cells using either Pepmute transfection reagent (Signagen) or Lipofectamine RNAiMAX (ThermoFisher Scientific) with 20 nM dsiRNA duplex directed against *FTO* (HSC.RNAI. N001080432.12.1, Integrated DNA Technologies) or 50 nM Silencer Select siRNA duplex pool targeting *ALKBH5* (s29686, s29687, s29688, ThermoFisher Scientific), respectively. Scrambled siRNA was used as non-targeting control.

FTO and ALKBH5 expression experiments were carried out in HEK293T cells using LipoD293 transfection reagent (Signagen) with Flag-tagged full length human wild-type FTO, human wild-type FTO containing a Flag tag and two nuclear export signals (NES) at the N terminus, GST-tagged ALKBH5 lacking 66 N-terminal amino acids, or respective control vectors.

Cells were maintained at 70-80% confluency and harvested 48-72 h after the transfection. Knockdown and overexpression were confirmed by western blot. Total RNA was isolated using TRIzol (ThermoFisher Scientific) according to the manufacturer's instructions. If indicated, two rounds of poly(A) mRNA enrichment from total RNA was carried out with oligo d(T)25 Magnetic Beads (NEB) according to the manufacturer's instructions.

Immunostaining of HEK293T cells

HEK293T cells transfected with either Flag-tagged full-length human wild-type FTO or human wild-type FTO containing two nuclear export signals (NES) at the N terminus were grown on cover slips coated with poly-d-lysine, fixed with 4% paraformaldehyde in PEM buffer (80 mM potassium PIPES, 5 mM EGTA, 2 mM $MgCl_2$, pH 7.0) for 10 min and permeabilized with 0.5% Triton X-100 in PEM buffer for 30 min. After blocking with 1% BSA in TBS-T for 1 h, cells were incubated with anti-DDDDK/Flag antibody (1:1,000 dilution in 1% BSA TBS-T) for 2 h followed by incubation with a goat anti-rabbit IgG antibody (1:1,000 dilution in 1% BSA TBS-T) for 1 h. Nuclei were stained with DAPI. All immunostaining steps were carried out at room temperature. Image acquisition was carried out on a Nikon Eclipse Ti microscope (Nikon), using NIS-Elements AR software (Version 3.2).

Generation of *DCP2* CRISPR knockout cells

DCP2-knockout cell lines were generated by CRISPR/Cas9 technology using two guide RNAs (gRNAs; 5′-UAUCAAAGACUAUAUUUGUA-3′ and 5′-AACCAGUUUCUUCAAAG ACC-3′) designed to target the *DCP2* genomic region corresponding to its catalytic site. Double-stranded DNA oligonucleotides corresponding to the gRNAs were inserted into the pSpCas9n(BB)-2A-Puro vector (Addgene). Equal amounts of the two gRNA plasmids were mixed and transfected into HEK293T cells using FuGENE 6 (Promega). The transfected cells were then subject to puromycin selection for three days and viable cells were used for serial dilution to generate single-cell clones. The genomic modification was screened by PCR and sequencing. In *DCP2*-knockout line 1, the two alleles were disrupted to generate out-of-frame mutation after V145 and I153, respectively. Line 2 contained a 55 nt homozygous deletion that removed the splicing site between intron 4 and exon 5. Line 3 contained one allele with a 194 nt deletion that removed the splicing site between intron 4 and exon 5, and the other allele was disrupted to generate out-of-frame mutation after V145. Loss of DCP2 protein expression was confirmed by western blot with in-house-generated anti-DCP2 sera[37].

Protein expression and purification

N-terminal HIS-tagged human FTO was generated by standard PCR-based cloning strategy and its identity was confirmed by sequencing FTO as described previously[4], with minor modifications. FTO was overexpressed in *E. coli* BL21 Rosetta (DE3) using pET-28(+) (Novagen). Cells expressing FTO were induced with 0.5 mM isopropyl (3-d-1-thiogalactopyranoside (IPTG) for 16 h at 18 °C. Cells were collected, pelleted and then resuspended in buffer A (50 mM NaH_2PO_4 pH 7.2, 300 mM NaCl, 20 mM imidazole-HCl pH 7.2, 5 mM (3-mercaptoethanol). The cells were lysed by sonication and then centrifuged at 10,000*g* for 20 min. The soluble proteins were purified using Talon Metal Affinity Resin (Contech) and eluted in buffer B (50 mM NaH_2PO_4 pH 7.2, 300 mM NaCl, 250 mM imidazole-HCl pH 7.2, 5 mM β-mercaptoethanol). Further concentration and purification was performed using Amicon Ultra-4 spin columns (Merck-Millipore). Recombinant protein was stored in enzyme storage buffer (20 mM HEPES pH 8.0, 50 mM NaCl, 10% glycerol) at -80 °C. All protein purification steps were performed at 4 °C.

Determination of relative m^6A_m, A_m and m^6A levels by thin layer chromatography

Levels of internal m^6A in mRNA were determined by thin-layer chromatography (TLC) essentially as previously described[4]. In brief, poly(A) RNA (100 ng) was digested with 2 units of RNase T1 (ThermoFisher Scientific) for 2 h at 37 °C in the presence of RNasin RNase Inhibitor (Promega). T1 cuts after every guanosine and exposes the 5′-hydroxyl of the following nucleotide, which can be A, C, U or m^6A. Thus, this method quantifies m^6A in a GA sequence context. 5′ ends were subsequently labelled with 10 units of T4 PNK (NEB) and 0.4 mBq [γ-^{32}P] ATP at 37 °C for 30 min followed by removal of the γ-phosphate of ATP by incubation with 10 units Apyrase (NEB) at 30 °C for 30 min. After phenol-chloroform extraction and ethanol precipitation, RNA samples were resuspended in 10 µl of DEPC-H_2O and digested to single nucleotides with 2 units of P1 nuclease (Sigma) for 3 h at 37 °C. 1 µl of the released 5′ monophosphates from this digest were then analysed by 2D TLC on glass-backed PEI-cellulose plates (MerckMillipore) as described previously[14].

The protocol to detect the m^6A_m:A_m ratio was based on the protocol developed by Fray and colleagues[14], with some modifications. Poly(A) RNA (1 µg) was used for the assay. Free 5′-OH ends were phosphorylated using 30 units of T4 polynucleotide kinase (PNK, NEB) and 1 mM ATP, according to the manufacturer's instructions. 5′ phosphorylated RNA fragments were digested with 2 units of Terminator 5′-Phosphate-Dependent Exonuclease (Epicentre). Capped RNAs are unaffected by this treatment. After phenol-chloroform extraction and ethanol precipitation, RNA samples were resuspended in 10 µl of DEPC-H_2O and 400 ng of the RNA was decapped with 25 units of RppH (NEB) for 3 h at 37 °C The 5′ phosphates of the exposed cap-adjacent nucleotide were removed by the addition of 5 units of rSAP (NEB) and further incubated for 30 min at 37 °C. Up to this point, all enzymatic reactions were performed in the presence of SUPERase In RNase Inhibitor (ThermoFisher Scientific). After phenol-chloroform extraction and ethanol precipitation, RNA samples were resuspended in 10 µl of DEPC-H_2O and 5′ ends were labelled using 30 units T4 PNK and 0.8 mBq [γ-^{32}P] ATP at 37 °C for 30 min. PNK was heat inactivated at 65 °C for 20 min and the reaction was passed through a P-30 spin column (Bio-Rad) to remove unincorporated isotope. 10 µl of labelled RNA were then digested with 4 units of P1 nuclease (Sigma) for 3 h at 37 °C. 4 µl of the released 5′ monophosphates from this digest were then analysed by 2D TLC on glass-backed PEI-cellulose plates (MerckMillipore) as described previously[14].

Signal acquisition was carried out using a storage phosphor screen (GE Healthcare Life Sciences) at 200 µm resolution and ImageQuantTL software (GE Healthcare Life Sciences). Quantification was carried out with ImageJ (V2.0.0-rc-24/1.49 m). For m^6A_m experiments, the m^6A_m:A_m ratio was calculated. The use of this ratio has been described previously[14]. We confirmed that this assay is linear by spotting twice the sample material and confirming that the signal intensity doubles for the unmodified nucleotides (A, C and U). Furthermore, exposure time of the TLC plates to the phosphor screen was chosen so that the signal was not saturated. For m^6A quantification, m^6A was calculated as a percentage of the total of the

A, C and U spots, as described previously[4]. The use of relative ratios for each individual sample is important since it reduces the error derived from possible differences in loading. To minimize the effects of culturing conditions on the measured m^6A_m/A_m ratios of each experimental group (for example, control versus knockdown), all replicates were processed in parallel to minimize any source of variability between samples being compared. Of note, the control conditions for siRNA transfection and plasmid transfection utilize different transfection reagents, which could affect baseline m^6A_m/A_m ratios.

In vitro decapping assays

22-nucleotide-long RNA oligonucleotides that have an A, A_m, m^6A or m^6A_m at their 5′ end were enzymatically capped with the vaccinia capping enzyme with [α-^{32}P]-N^7-methylguanosine triphosphate (m^7GTP) as previously described[38]. Decapping reactions were carried out according to ref. 38. In brief, 10 nM recombinant DCP2 protein was incubated with the indicated cap-labelled RNAs in decapping buffer (10 mM Tris-HCl pH 7.5, 100 mM KCl, 2 mM $MgCl_2$, 2 mM DTT, 0.5 mM $MnCl_2$, 40 U ml^{-1} recombinant RNase inhibitor) and incubated at 37 °C for 30 min. Reactions were stopped with 25 mM EDTA at the indicated time points. The identity of decapping products of the indicated modified cap adenosines subjected to 20 nM recombinant human DCP2 protein at 37 °C for 30 min were confirmed to be m^7GDP by treatment with 0.5 U nucleoside diphosphate kinase (NDPK) at 37 °C for 30 min in the presence of 0.5 mM ATP. A cap labelled RNA with a guanosine as the first nucleotide generated as previously described[38] was used as a positive control. Decapping products were resolved by PEI-cellulose TLC plates (Sigma-Aldrich) and developed in 0.45 M $(NH_4)_2SO_4$ in a TLC chamber at room temperature. Reaction products were visualized and quantitated with a Molecular Dynamics PhosphorImager (Storm860) with ImageQuant-5 software.

Synthesis of mRNAs with specific forms of methylated caps

To generate mRNAs that begin with either m^7GpppA_m or $m^7Gpppm^6A_m$, we used thermostable TGK polymerase[39], which enables RNA synthesis with an RNA primer from a DNA template. The primers contained either m^7GpppA_m or $m^7Gpppm^6A_m$ as the extended cap. The use of TGK polymerase and specific methylated forms of the primer ensures that all synthesized mRNAs begin with the desired extended cap structure. The DNA template for RNA synthesis was prepared by PCR using the pNL1.1[*Nluc*] vector (Promega) as a template and Phusion High-Fidelity PCR Master Mix (NEB). Since the template needs to be single-stranded, we used a strategy of selectively degrading one of the strands of the PCR product. To achieve this, PCR was performed with a 5′-phosphorylated forward primer and a 5′-OH reverse primer. The undesired 5′-phosphorylated strand was digested with lambda exonuclease (Lucigen) (1 U per 1–2 µg double-stranded DNA) for 2 h at 37 °C. The digestion was stopped by phenol chloroform extraction and ethanol precipitation of the single-strand template.

RNA forward synthesis was performed from either an m^7GpppA_m (20 nt) or an $m^7Gpppm^6A_m$ (20 nt) primer in a 50 µl reaction consisting of 1 × Thermopol buffer (NEB) supplemented with 3 mM MgSO4 and 2.5 mM NTP with a 1:1 primer/ template ratio at 100 pmol each and 150 nM TGK polymerase. The primer extension was performed at two cycles of 10 s at 94 °C, 1 min at 50 °C, and 1 h at 65 °C. After RNA synthesis, the template DNA strand was degraded using TURBO DNase (Thermo Fisher Scientific) and the capped nLuc mRNAs were purified with an RNeasy column (Qiagen). An approximately 250 nt poly(A) tail was added with A-Plus Poly(A) Polymerase Tailing Kit (Cellscript). The polyadenylated mRNAs were purified with oligo d(T)25 Magnetic Beads (NEB) according to the manufacturer's instructions.

Electroporation of mRNA

To deliver m^7GpppA_m-nLuc and $m^7Gpppm^6A_m$-nLuc mRNAs into HEK293T cells, we used electroporation. HEK293T cells were trypsin-ized and resuspended in Ingenio Electroporation Solution (Mirus) at 5×10^6 cells ml^{-1}. 100 μl of cell suspension was added to 2 μg of mRNA. Electroporation was carried out with Nucleofector II (Amaxa) using program Q-001. The cell suspension was immediately transferred to 37 °C pre-warmed growth medium supplemented with 5 mM $CaCl_2$ and 200 U ml^{-1} micrococcal nuclease (Clontech). After a 15 min incubation period at 37 °C to remove any residual extracellular RNA, cells were transferred to 24-well plates at 1.25×10^5 and incubated until adherent. Cells were then either collected immediately or after 2 h of incubation for RNA extraction and quantification by qRT-PCR.

RNA half-life measurement after transcriptional inhibition

RNA half-lives after transcriptional inhibition were determined essentially as previously described[40,41]. In brief to achieve transcriptional inhibition for calculation of mRNA half-life, Flag- and NES-FTO-transfected HEK293T cells were either left untreated (that is, 0 h time point) or treated with actinomycin D (Sigma) for 6 h at a final concentration of 5 μg ml^{-1}. Cells were then harvested for RNA isolation using TRIzol (Thermo Fisher Scientific). The total RNA derived from Flag- and NES-FTO-transfected HEK293T cells, was spiked-in with ERCC RNA controls (Ambion) before the isolation of mRNA and RNA-seq (see below). Read count tables were generated using STAR aligner[42]. DESeq2[43] was used to calculate ERCC spike-in RNA size factors, which were then applied to normalize for library size changes in each replicate. As shown in Extended Data Fig. 6c, the half-lives derived from the transcriptional inhibition experiments showed high correlation between independent replicates.

RNA half-life measurements by 5-bromouridine (BrU) pulse-chase

RNA half-life measurements by BrU pulse-chase was carried out essentially as described previously[44]. Briefly, HEK293T cells were pulsed with 150 μM 5-bromouridine (Santa Cruz Biotechnology) for 24 h. Chase was initiated by changing to medium containing 1.5 mM uridine (Sigma) and cells were collected for RNA extraction after 6 and 16 h. BrU-pulsed cells without uridine-chase were used as basal (0 h) controls. Total RNA was extracted with TRIzol reagent (Thermo Fisher Scientific) according to the manufacturers instructions. Immunoprecipitation of BrU-labelled RNA from total RNA was carried out as previously described[44]. A BrU-labelled NanoLuc luciferase (nLuc) RNA was generated by *in vitro* transcription as previously described[44] and used as a spike-in immunoprecipitation control at 10 pgp per 1 μg input RNA.

Quantitative real-time PCR

1–2 μg total RNA or 500 ng BrU-labelled RNA was reverse transcribed using the High Capacity cDNA Kit (Thermo Fisher Scientific) according to the manufacturer's instructions. The cDNA was subjected to quantitative real-time PCR analysis with the TaqMan Gene Expression Master Mix (Thermo Fisher Scientific) using Taqman Gene Expression Assays (Thermo Fisher Scientific) on a ViiA 7 Realtime-PCR System (Thermo Fisher Scientific). The following predesigned Taqman Gene expression assays were used in the current study: *FUCA1* (Hs00609173_m1), *MAGOHB* (Hs00970279_m1), *PCNA* (Hs00427214_g1), *PCK1* (Hs01572978_g1), *PSMD3* (Hs00160646_m1), *SCFD2* (Hs00293797_m1).

ACTB (Hs01060665_g1) was used as a housekeeping gene to normalize the level of transfected nLuc mRNA. A custom probe and primer set was designed to detect nLuc cDNA (forward 5′-ATGTCGATCTTCAGCCCATTT-3′; reverse 5′-GGA GGTGTGTCCAGTTTGTT-3′; probe 5′-/56-FAM/ATCCAAAGGATTGTC CTGAGCGGT/3IABkFQ/-3′). Amplification of nLuc cDNA was linear over seven orders of magnitude. The $2^{-\Delta\Delta C_t}$ method was used to calculate relative gene expression changes between time points and biological replicates.

m^6A peak enrichment analyses

m^6A peaks were based on our previous MeRIP-seq analysis of *Fto*-knockout midbrain tissue[11]. For analysis of m^6A peak distribution, m^6A peaks were individually binned based on their location within mRNA and mapped onto a virtual transcript in a metagene analysis to show their collective distribution within mRNA. Bin numbers were chosen such that each bin is on average 50 nucleotides long. Peak counts were smoothed using a spline function. We weighted each peak by a coefficient corresponding to the number of MeRIP-seq reads in the immunoprecipitated samples relative to the reads obtained before immunoprecipitation. This peak mass value represents the enrichment of methylated mRNA at individual m^6A sites after immunoprecipitation and reflects the degree to which an mRNA is methylated at a particular m^6A site. To generate the peak height ratio plot, we used ratios between *Fto*-knockout peak mass over wild-type peak mass. The same bin numbers and sizes were used for all analyses.

Mapping and validation of m^6A_m sites

To further increase the number of miCLIP-based detection of m^6A_m sites, we used the miCLIP pipeline[12] with the following modifications. Raw miCLIP reads were trimmed of their 3′ adaptor and demultiplexed as previously described[12]. Then, PCR-duplicated reads of identical sequences were removed using the pyDuplicateRemover.py script of the pyCRAC tool suite (version 1.2.2.3). Unique reads were mapped with Bowtie (version 1.1.1) to hg19. Files of aligned reads were processed with samtools (version 1.2), bedtools (version 2.25.0), and custom bash commands to derive the 5′ ends of each aligned read. 5′-end coordinates of the reads were then combined into ‘piles’ at each single nucleotide throughout the genome using the tag2cluster.pl script of the CIMS software package[45] (parameters: -v -s -maxgap “-1”). Piles were then filtered to contain at least five 5′ ends at a single nucleotide. Adjacent piles (zero nucleotides apart) were clustered together using a custom perl script. The resulting clusters were annotated with their transcript ID and transcript region (5′ UTR, CDS, or 3′ UTR) using a custom perl script and custom bash commands. After annotation, clusters were filtered for those found in the 5′ UTR of annotated mRNAs. To remove noise, clusters with a width of one nucleotide were removed using custom bash commands. Finally, custom bash commands were used to filter for clusters found only at the very beginning of 5′ UTRs.

To verify that these are indeed m^6A_m residues, we took advantage of fact that m^6A_m occurs only at transcription start sites (TSS). Thus, we compared the known TSS and transcription initiation sequences around each m^6A_m-containing region. To identify genome-wide positions of the TSS from published CAGE-seq datasets[16] and genome-wide positions of the consensus initiator motif, YYANW (Y = C or T, *N* = A, C, G, or T, W = A or T)[46], a custom perl script was used. The CAGE sites in this data set are combined from RLE (relative log expression)-normalized robust CAGE-seq analysis of multiple cell lines and tissues, and therefore provide high sensitivity for detecting transcription start sites.

We then determined the distribution of TSS or the YYANW sequence around m^6A_m-containing regions. To do so, we used the 'closest' tool of the bedtools suite to determine distances between each m^6A_m-containing region and the nearest TSS or YYANW sequence. The following commands were used to find TSS or YYANW sequences nearest to the 5′-most nucleotide of each m^6A_m-containing region.

To measure the distance of TSS or YYANW sequences that overlap with m^6A_m-containing regions:

```
bedtools closest -a m6Am.reference.points.bed -b feature.locations.bed -s > m6Am.distance.overlap.bed
```

To measure the distance of TSS or YYANW sequences that do not overlap with m^6A_m-containing regions:

```
bedtools closest -a m6Am.reference.points.bed -b TSS.locations.bed -s -io > m6Am.feature.distance.bed
```

The total distributions of the distances of TSS or YYANW sequences to m^6A_m-containing regions (regardless of overlap) were then plotted as a histogram.

These results demonstrated that TSS and the YYANW core initiator sequence are highly clustered at m^6A_m-conaining regions. This suggests that the called m^6A_m-containing regions reflect true transcription initiation sites. All newly identified m^6A_m mRNAs are listed in Supplementary Table 1 together with CAGE and initiator overlap. Notably, m^6A_m sites are distinct from the recently described 5′ UTR m^6A sites[23] since they are found in a different sequence context and overlap with transcription start sites[12]. Furthermore, the previously described *ex vivo* m^1A to m^6A conversion is unlikely to generate artefacts during m^6A mapping. m^1A to m^6A conversion requires extreme conditions[47] that are not used in miCLIP or MeRIP-seq. Additionally, m^6A peaks are not detected at the annotated m^1A site in the 28S rRNA[12], indicating that no detectable m^1A to m^6A conversion is occurring during miCLIP.

At present, it is not possible to determine the absolute stoichiometry of m^6A_m or A_m at the first position of mRNA at a transcriptome-wide level. Conceivably, if the stoichiometry of m^6A_m is not 100% on a specific m^6A_m-classified mRNA, the effect of m^6A_m may be underestimated. For experiments using BrU pulse-chase labelling, we sought to examine mRNAs with high stoichiometry m^6A_m. As a surrogate for stoichiometry, we measured the miCLIP/RNA-seq ratio in a 20 nt window surrounding the 5′ m^6A_m region using bedtools coverage. For qRT-PCR analysis in the BrU pulse-chase experiments examining individual mRNA half-life changes upon NES-FTO expression, m^6A_m mRNAs with high miCLIP/RNA-seq ratio were chosen (Supplementary Table 5).

Classification of mRNAs based on the first nucleotide

In experiments where we compared m^6A_m-intiated mRNAs to A_m-, C_m-, G_m- and U_m-initiated mRNAs, we classified the mRNAs based on the nucleotide at the annotated TSS. Annotated TSS were extracted from the Ensembl BioMart database[48]. A complete list of transcripts with their respective annotated transcription start site is found in Supplementary Table 2.

Metagene analysis using miCLIP reads

For Extended Data Figs 6f g, we generated a high-coverage m^6A individual-nucleotide-resolution cross-linking and immunoprecipitation (miCLIP) data set in HEK293T cells[12]. Metagenes were constructed for the miCLIP-identified unique 6mA reads using an in-house perl annotation pipeline and custom R scripts. Briefly, the 6mA reads were mapped to different RNA features (5′ UTR, CDS and 3′ UTR) of the human genome (hg19). Position of the reads was normalized to the median feature length of the RNAs to which the tag mapped. A frequency distribution plot was generated by counting number of reads in contiguous bins on a virtual mRNA transcript, whose feature lengths represent the median feature lengths of RNAs under analysis either of each individual sample or of the control sample. A kernel density (Gaussian) estimate was plotted.

RNA-seq analysis

To avoid potential clonal variation, 10^6 cells from each of the three DCP2 CRISPR lines were pooled together (referred to as *DCP2*-knockout cells), passaged once, and immediately used for RNA-seq. The DCP2 CRISPR line RNA samples were subject to depletion of ribosomal RNA using RiboMinus Eukaryote System v.2 (Life Technologies), followed by cDNA library preparation using the Illumina TruSeq RNA Sample Preparation Kit v.2. The sequencing (2 × 100-bp paired-end) was performed by RUCDR Infinite Biologics (Piscataway) using the Illumina Hiseq 2500 according to the manufacturer's protocol. Two independent biological replicates were sequenced for each condition. The RNA-seq library for miCLIP normalization (see 'Mapping and validation of m^6A_m sites') was prepared using a cloning strategy parallel to the one used in miCLIP[12,49].

For all other RNA-seq analyses, total RNA was diluted to a concentration of 50 ng μl^{-1} and submitted to the Weill Cornell Medicine Epigenomics Core for isolation of mRNA and library preparation using the Illumina TruSeq Stranded mRNA Library Prep Kit (RS-122-2101, Illumina). The libraries were sequenced on the Illumina HiSeq 2500 instrument, in either single-read or paired-end mode, with 50-100 bases per read. At least two independent biological replicates were sequenced for each condition.

Gene expression was measured using STAR[42] read counts (version 2.4.1; -quantMode TranscriptomeSAM GeneCounts), which were processed with either the DESeq2 pipeline[43] (version 1.8.1) or the RSEM pipeline[50] (version 1.2.25). Analysis and visualization of RNA-seq datasets was carried out with custom in-house-generated R scripts using RStudio (Version 0.99.489). Only transcripts with normalized read counts > 1 were included in the analyses.

Previously published RNA-seq datasets used in the current study were extracted from Gene Expression Omnibus (GEO, NCBI) and, if no processed data was available, the fastq files were reanalysed with the pipelines described above. mRNA half-life data was either calculated based on the decay rates derived from our own HEK293T cell data set or was extracted from previously published half-life data sets in HeLa cells[40]. Only mRNAs with a half-life between 0 h and 25 h were used in our analysis of mRNA half-life based on the identity of the first encoded nucleotide. For classification of short- and long-lived mRNAs, half-life values were divided into quartiles. mRNAs in the lowest quartile (0–3 h) were defined as short-lived, whereas mRNAs in the highest quartile (10–24 h) were defined as long-lived. The analysis of *DICER*- and *AGO2*-knockdown effects on m^6A_m mRNAs was performed using previously published datasets[20]. We used m^6A_m mapped in mouse liver[12] in order to correspond with the mouse liver expression analysis in these datasets. When indicated, we limited the analysis to mRNAs with TargetScan-predicted microRNA-binding sites and a context score cut-off ≤ 0.1 (ref. 51). Non-target mRNAs in Extended Data Fig. 9f were filtered for mRNAs that contain 3′ UTR sizes ≤300 nt to reduce the likelihood of analysing mRNAs with alternative 3′ UTRs or alternative polyadenylation sites. The analysis of the effect of single microRNA transfection on m^6A_m mRNAs was performed using previously published datasets of miR-155 duplex transfected HeLa cells[21]. In these experiments, we limited the analysis to CLIP-supported microRNA-mRNAs interactions according to starBase v.2.0[52].

Ribosome profiling

To determine if m^6A_m is associated with changes in translation efficiency, we analysed a previously published ribosome profiling dataset[53]. Ribosome footprint reads and corresponding RNA-seq reads were processed essentially as described[54]. First, adaptors were trimmed using Flexbar v.2.5. For ribosome footprints, only reads from which the adaptor was trimmed were retained. Reads mapping to ribosomal RNAs were removed with bowtie v.1.1.2. Remaining reads were then aligned to the hg19 genome with STAR v.2.5.2a in a splicing-aware manner and using UCSC refSeq as a transcript model database (version from 2 June 2014 downloaded from Illumina iGenomes). Two mismatches were allowed and only unique alignments were reported. Aligned reads were then counted on transcript regions using custom R scripts considering only transcripts with annotated 5′ and 3′ UTRs. Translation efficiency was calculated as previously described[21], with pre-filtering for transcripts that had at least ten counted reads.

Statistics and software

P values were calculated with a two-tailed unpaired Student's *t*-test or, for the comparison of more than two groups, with a one- or two-way ANOVA followed by Bonferroni's or Tukey's post hoc test. Reproducibility of half-life and translation efficiency measurements was assessed by calculating the Pearson correlation coefficient between replicates. The influence of covariates on the effect of m^6A_m-containing mRNAs compared to non-m^6A_m mRNAs on mRNA half-life was studied by ANCOVA analysis using SPSS Statistics software (IBM, v. 22). The covariates include the number of mRNA-destabilizing AU-rich, GU-rich and U-rich elements[55], gene expression (log2[FPKM], FPKM > 1), translation efficiency ($\log_2$[TE], TE > 0), GC composition and length of 5′ and 3′ UTR, number of exons in 5′ and 3′ UTRs, number of conserved miRNA target sites ($P_{CT} > 0$)[56], minimum-free energy to length ratio[57], and the number of G-quadruplexes in the 5′ UTR[58,59]. GC composition, UTR lengths, and the number of exons were calculated from refseq mRNA annotations (hg19) from the UCSC Genome browser. *P* values of 0.05 or less were considered significant. Initial reaction velocities for enzyme kinetics were analysed by nonlinear regression curve-fitting using Graphpad Prism software (version 5.0f) to obtain k_{cat}, K_m and V_{max}. Gene Ontology (GO) functional annotation was performed using PANTHER Overrepresentation Test (release 20150430) and Bonferroni correction with a *P* value threshold of <0.01. Non-m^6A_m-containing mRNAs were used as the background gene list.

Code availability

The custom Perl and R scripts used in this study are available on request from the corresponding author (S.R.J.).

Data availability

Sequencing data that support the findings of this study have been deposited in the GEO database under accession number GSE78040. A summary of all the data sets used in the current study can be found in Supplementary Table 6.

Extended Data

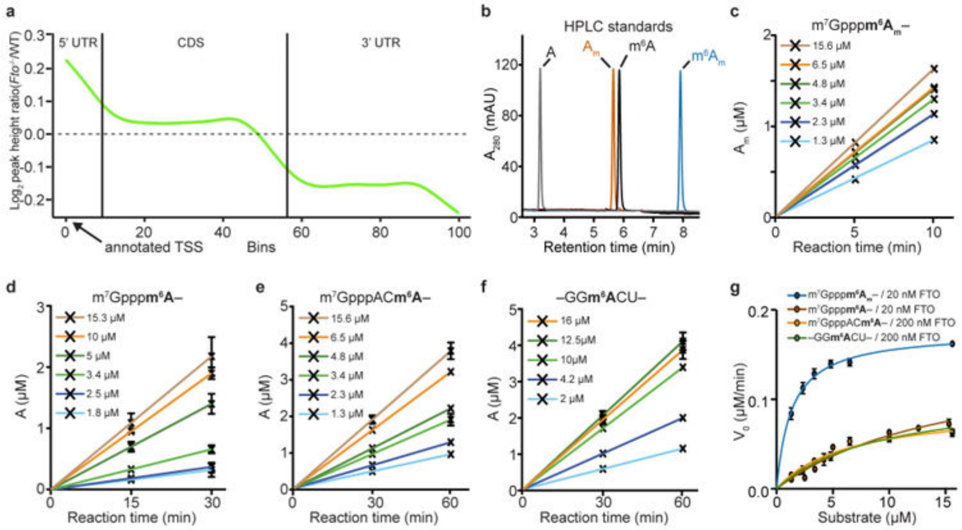

Extended Data Figure 1. m^{6}A enrichment is increased within the 5′ UTR of *Fto*-knockout mice relative to wild-type mice and FTO prefers m^{6}A$_m$ over m^{6}A

a, m^{6}A peak mass was calculated for all peaks that were found in both *Fto*-knockout mice (*Fto*$^{-/-}$) and wild-type (WT) mice. The ratio of each individual peak's mass relative to the average peak mass for each sample was then determined, providing a relative peak mass. The relative peak mass for *Fto*$^{-/-}$ mice was divided by the relative peak mass for wild-type mice for each m^{6}A peak. A metagene analysis was performed to plot the distribution of these peak mass ratios (knockout/wild type) along the length of an mRNA. This analysis reveals that the changes in peak mass ratio for knockout mice relative to wild-type mice are increased in the 5′ UTR. These findings provided the first hint that FTO activity might be directed towards m^{6}A$_m$. The basis for the reduced peak mass ratio in the 3′ UTR is unclear. Because FTO is a demethylating enzyme, loss of FTO should increase nucleotide methylation. Thus, the reduced methylation of m^{6}A residues in the 3′ UTR is likely to be an indirect effect of FTO deficiency. CDS, coding sequence; TSS, transcription start site. **b**, Representative HPLC chromatogram of synthetic standards that were used to determine retention times of adenosine (A), 2′-*O*-methyladenosin (A$_m$), *N*^{6}-methyladenosine (m^{6}A), or *N*^{6},2′-*O*-dimethyladenosine (m^{6}A$_m$). mAU, milli absorbance units. **c**-**f**, Reaction curves for FTO with the different substrates that were used to calculate reaction velocity for Michaelis-Menten analysis. FTO concentrations that allowed initial velocity conditions were used for individual oligonucleotides (20 nM FTO for m^{7}Gpppm^{6}A$_m$ (**c**) and m^{7}Gpppm^{6}A (**d**); 200 nM FTO for m^{7}Gpppm^{6}A (**e**) and internal m^{6}A (**f**) in a GGACU context; $n = 3$ biological replicates; mean ± s.e.m.). **g**, Michaelis-Menten plots of FTO for either m^{6}A$_m$ or m^{6}A. Michaelis-Menten curves of FTO reacting with m^{7}Gpppm^{6}A$_m$ (blue), m^{7}Gpppm^{6}A (brown), m^{7}GpppACm^{6}A (orange) or m^{6}A in a GGACU context (green). Owing to the increased reaction speed of FTO with m^{6}A$_m$ and m^{6}A adjacent to the m^{7}G compared to more distal m^{6}A, the enzyme concentration was tenfold lower when we assessed reaction rates for m^{6}A$_m$ (20 nM FTO for the m^{7}Gpppm^{6}A$_m$ and m^{7}Gpppm^{6}A oligonucleotide; 200 nM FTO for the m^{7}Gpppm^{6}A and for internal m^{6}A in a GGACU context). Figure 1d shows a plot in which the data are normalized to enzyme concentration. However, here the plot shows data that were not normalized to enzyme concentration (*n* = 3 biological replicates; mean ± s.e.m.).

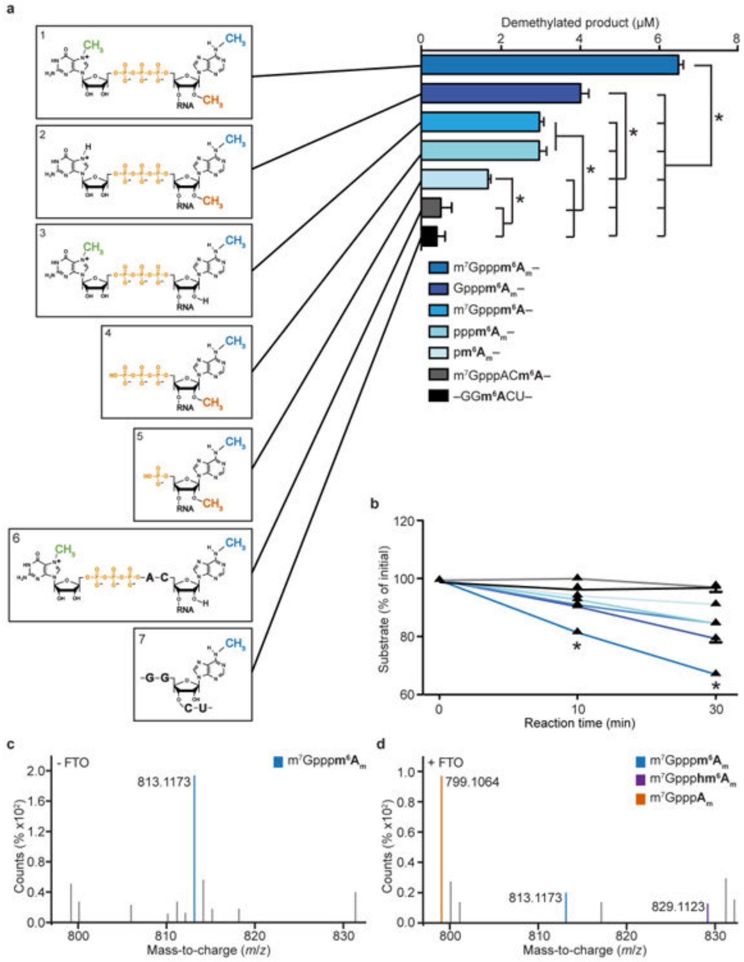

Extended Data Figure 2. FTO-mediated demethylation of m^6A_m depends on integral parts of the mRNA 5′ cap and accurate mass measurement of the oxidative demethylation of the extended $m^7Gpppm^6A_m$-cap by FTO

a, Structure-activity relationship of FTO and its substrate. ALKBH5 preferentially demethylates m^6A in its physiological sequence context but FTO does not require a sequence context to demethylate m^6A (refs 3,60). This lack of a sequence preference suggests that m^6A is not a preferred substrate for FTO. We therefore asked whether FTO preferentially demethylates m^6A_m in its natural sequence context as the first nucleotide adjacent to the m^7G cap. To determine the specific structural elements of the extended cap that are required for efficient N^6-demethylation of m^6A_m, we synthesized oligonucleotides with different 5′ ends indicated in boxes 1-7. Shown is the amount of product (A_m for substrates 1, 2, 4, 5; A for substrates 3, 6, 7) generated by FTO (200 nM) after 30 min when incubated with different oligonucleotides (20 μ*M)* containing m^6A_m or N^6-methyladenosine (m^6A). The highest FTO demethylation activity on was on the full cap1m structure $m^7Gpppm^6A_m$ (1). Removal of the N^7-methyl from the guanosine (2) reduced FTO activity by 30% (2), whereas removal of either the 2′-*O*-methyl from the adenosine (3) or the m^7G

(4) resulted in a 50% activity loss. FTO activity was further reduced by removal of m^{7}Gpp (5). The lowest FTO demethylation activity was observed when using m^{6}A as a substrate, either at the +3 position after the cap (6) or internally in a GGACU context (7). Thus, an adjacent m^{7}G cap does not activate m^{6}A as a substrate for FTO. These results indicate that FTO activity is dependent on the presence of a full cap structure, including the 2′-*O*-methyl at the +1 position, whereas m^{6}A is a poor substrate for FTO (one-way ANOVA with Tukey's post hoc test; $*P < 0.001$; $n = 3$ biological replicates; mean ± s.e.m.). **b**, Structure-activity relationship of FTO and its substrate. Shown is the amount of substrate converted by FTO in a time-dependent manner at the same reaction conditions as in a (two-way ANOVA with Tukey's post hoc test; $*P < 0.001$ versus all other structures; $n = 3$ biological replicates; mean ± s.e.m.). **c**, **d**, FTO demethylates m^{7}Gpppm^{6}A$_m$ at the N^6-position through oxidization of m^{7}Gpppm^{6}A$_m$ to an N^6-hydroxymethyl intermediate (m^{7}Gppphm^{6}A$_m$). The final reaction product is m^{7}GpppA$_m$. Liquid chromatography/mass spectrometry analysis of m^{7}Gpppm^{6}A$_m$ RNA either left untreated (**c**; —FTO) or after incubation with 3 μM FTO for 10 min (**d**; +FTO). Shown are representative mass-to-charge *(m/z)* ratios of precursor ions. In the absence of FTO, the dinucleotide shows a measured *m/z* ratio of 813.1173, 0.98 p.p.m. mass accuracy from the exact *m/z* of 813.1165 (formula $C_{23}H_{33}N_{10}O_{17}P_3$). Incubation with FTO generates m^{7}Gppphm^{6}A$_m$, shown as a measured *m/z* of 829.1123, 1.01 p.p.m. mass accuracy from the exact m^{7}Gppphm^{6}A$_m$ *m/z* of 829.1114 (formula $C_{23}H_{33}N_{10}O_{18}P_3$). The demethylated final product m^{7}GpppA$_m$ and residual non-demethylated m^{7}Gpppm^{6}A$_m$ were also detected in the FTO reaction mixture, with m^{7}GpppA$_m$ showing a measured *m/z* of 799.1064, 6.9 p.p.m. mass accuracy from the exact *m/z* of 799.1009 (formula $C_{22}H_{31}N_{10}O_{17}P_3$).

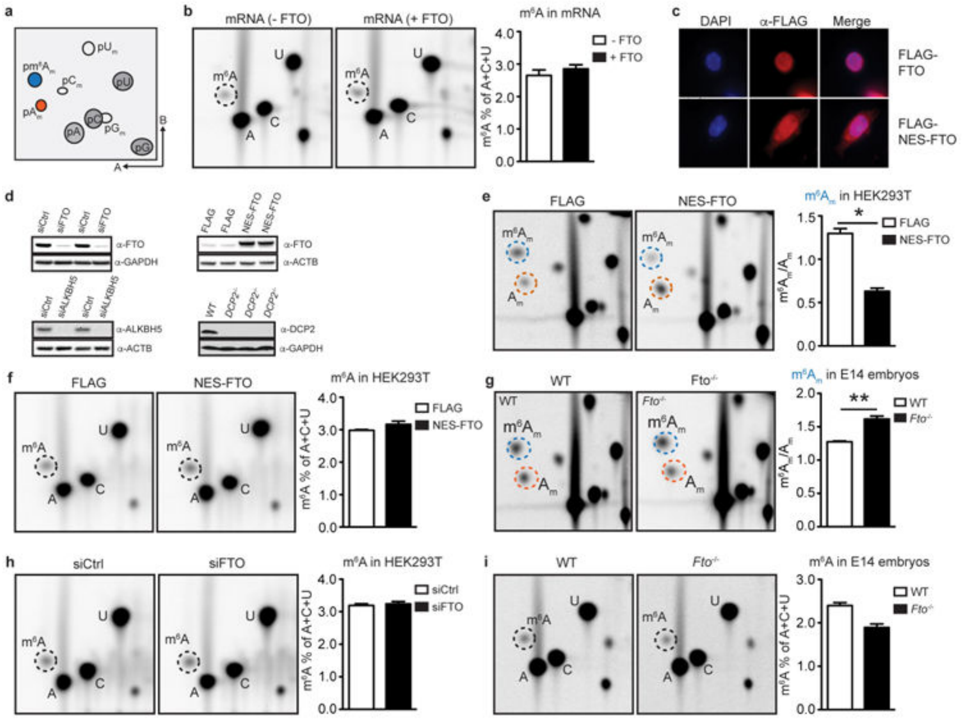

Extended Data Figure 3. ^{6}A$_m$ is the preferred substrate for FTO *in vivo*

a, Modifications of the extended mRNA cap. The first nucleotide adjacent to the m^{7}G and the 5′-to-5′-triphosphate (ppp) linker is subjected to 2′-*O*-methylation (orange) on the ribose, forming cap1. Cap1 can be further 2′-*O*-methylated at the second nucleotide to form cap2 (not depicted here). If cap1 contains a 2′-*O*-methyladenosine (A$_m$), it can be further converted to cap1m by *N*^{6}-methylation (blue), which results in *N*^{6},2′-*O*-dimethyladenosine (m^{6}A$_m$). **b**, Relative abundance of m^{6}A in mRNA treated with recombinant FTO. Internal m^{6}A residues that follow G in mRNA can be labelled and quantified in a 2D TLC method[61]. The relative abundance of m^{6}A versus (A + C + U) in 400 ng mRNA that was either left untreated (—FTO) or incubated for 1 h with 1 *μM* bacterially expressed recombinant human FTO (+FTO) was determined by 2D TLC. We did not observe any decrease of m^{6}A in FTO-treated mRNA, indicating that FTO does not efficiently demethylate m^{6}A in its physiological context in mRNA *in vitro* (representative images shown; *n* = 3 biological replicates; mean ± s.e.m.). **c**, FTO with a nuclear export signal is localized in the cytoplasm. Immunofluorescence staining of DDDDK/Flag tag in HEK293T cells transfected with Flag-tagged wild type FTO (Flag-FTO) or Flag-tagged FTO with an N-terminal nuclear export signal (NES-FTO). FTO is primarily nuclear while NES-FTO is readily detected in the cytosol. DAPI was used to stain nuclei (representative images shown). **d**, Western blot analyses were performed to verify successful knockdown, overexpression and knockout. Top left, cell extracts from HEK293T cells with *FTO* knockdown were blotted with anti-FTO antibody. Knockdown efficiency was approximately 75%. The cell extracts were from the same samples used for RNA-seq analysis in Fig. 3d. GAPDH was used as loading control. Top right, western blot analysis of HEK293T expressing Flag vector (Ctrl) or FTO with an N-terminal nuclear export signal (NES-FTO) that were used for RNA-seq half-life analysis in Fig. 3c. An antibody directed against β-actin was used as a loading control. The lower band represents endogenous FTO, whereas the upper band represents exogenous NES-FTO, which showed approximately tenfold overexpression. Top left, cell extracts from *ALKBH5*-knockdown HEK293T cells with were blotted with anti-ALKBH5 antibody. Knockdown efficiency was approximately 90%. The cell extracts were from the same samples used for RNA-seq analysis in Extended Data Fig. 7e. β-Actin was used as loading control. Top right, western blot analysis of three different HEK293T clonal lines with CRISPR-mediated knockout of *DCP2* that were used for RNA-seq analysis. GAPDH was used as a loading control. **e**, FTO expression decreases m^{6}A$_m$ in HEK293T cells. The relative abundance of modified adenosines in mRNA caps of HEK293T expressing Flag vector (Ctrl) or Flag-tagged FTO with an N-terminal nuclear export signal (Flag-NES-FTO) was determined by 2D TLC. When determining the ratio of m^{6}A$_m$ to A$_m$, we observed a significant decrease of m^{6}A$_m$ in Flag-NES-FTO-overexpressing cells, indicating that FTO can convert cytoplasmic m^{6}A$_m$ to A$_m$ *in vivo*. Notably, the ratios of m^{6}A$_m$:A$_m$ that we observed upon FTO expression (both with and without the NES) may under-represent the true effect of FTO: A$_m$ mRNAs are generally less stable than m^{6}A$_m$ mRNAs owing to their degradation in cells via DCP2-mediated pathways (see Figs 3 and 4). Thus the A$_m$ mRNAs generated by FTO-mediated demethylation of m^{6}A$_m$ may not efficiently accumulate in cells compared to m^{6}A$_m$ mRNAs (representative images shown; *n* = 3 biological replicates; mean ± s.e.m.; unpaired Student's *t*-test, $^*P \leq 0.01$). **f**, FTO expression does not affect m^{6}A in HEK293T cells. The relative abundance of m^{6}A versus (A + C + U) in mRNA of HEK293T expressing empty vector (Ctrl) or FTO with an N-terminal nuclear export signal (NES-FTO) was determined by 2D TLC. We did not observe any decrease of m^{6}A upon NES-FTO expression, indicating that FTO does not readily influence levels of m^{6}A in HEK293T cells at this level of expression. Notably, under these same expression conditions, m^{6}A$_m$ is readily demethylated (see Extended Data Fig. 3e) (representative images shown; *n* = 3 biological replicates; mean ± s.e.m.). Control experiments measuring m^{6}A and m^{6}A$_m$ levels following *ALKBH5*-knockdown and expression in HEK293T cells are shown in Extended Data Fig. 4. **g**, FTO deficiency increases m^{6}A$_m$ *in vivo.* Relative abundance of modified adenosines in mRNA caps of embryonic day (E) 14 wild-type (WT) littermate controls and *Fto* knockout *(Fto$^{-/-}$)* mouse embryos (representative images shown; *n* = 3 biological replicates; mean ± s.e.m.; unpaired Student's *t*-test, $^{**}P \leq 0.01$). **h**, *FTO* knockdown does not affect m^{6}A in HEK293T cells. The relative abundance of m^{6}A versus (A + C + U) in mRNA of HEK293T cells transfected with scrambled siRNA (siCtrl) or siRNA directed against FTO (siFTO) was determined by 2D TLC. We did not observe any increase of m^{6}A upon *FTO* knockdown, indicating that FTO does not readily influence levels of m^{6}A *in vivo* (representative images shown; *n* = 3 biological replicates; mean ± s.e.m.). **i**, Relative abundance of m^{6}A in *Fto*-knockout mouse embryos. The relative abundance of m^{6}A versus (A + C + U) in mRNA of embryonic day 14 wild-type littermate controls and *Fto*-knockout (*Fto*$^{-/-}$) mouse embryos was determined by 2D TLC. We did not observe any increase of m^{6}A in *Fto*-deficient embryos, indicating that FTO does not influence the levels of m^{6}A in this embryonic stage (representative images shown; *n* = 3 biological replicates; mean ± s.e.m.).

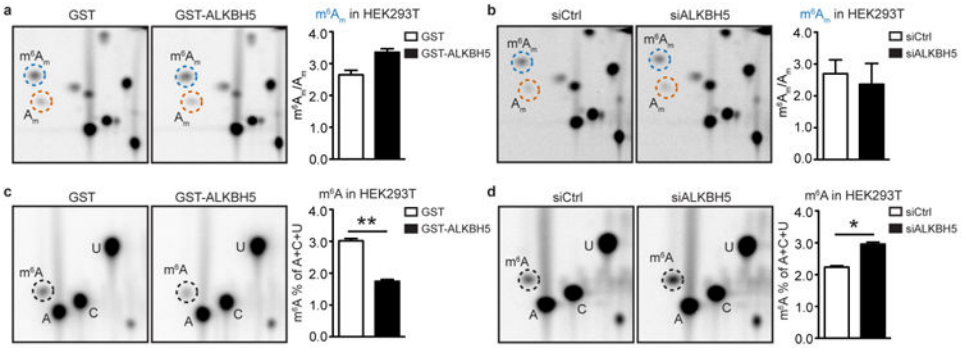

Extended Data Figure 4. ALKBH5 demethylates m^{6}A but not m^{6}A$_m$ in mRNA in HEK293T cells

a, ALKBH5 expression does not decrease m^{6}A$_m$ in HEK293T cells. The relative abundance of modified adenosines in mRNA caps of HEK293T cells expressing GST vector (Ctrl) or ALKBH5 with an N-terminal GST tag (GST–ALKBH5) was determined by 2D TLC. When determining the ratio of m^{6}A$_m$ to A$_m$, we did not observe a significant decrease of m^{6}A$_m$ in ALKBH5-overexpressing cells, indicating that ALKBH5 does not convert m^{6}A$_m$ to A$_m$ *in vivo* (representative images shown; *n* = 3 biological replicates; mean ± s.e.m.). **b**, *ALKBH5* knockdown does not increase m^{6}A$_m$ in HEK293T cells. The relative abundance of modified adenosines in mRNA caps of HEK293T cells transfected with scrambled siRNA (siCtrl) or siRNA directed against ALKBH5 (siALKBH5) was determined by 2D TLC. When determining the ratio of m^{6}A$_m$ to A$_m$, we did not observe a significant increase of m^{6}A$_m$ in ALKBH5-expressing cells, indicating that ALKBH5 does not convert m^{6}A$_m$ to A$_m$ *in vivo* (representative images shown; *n* = 3 biological replicates; mean ± s.e.m.). **c**, *ALKBH5* knockdown increases m^{6}A in HEK293T cells. The relative abundance of m^{6}A versus (A + C + U) in mRNA of HEK293T cells transfected with scrambled siRNA (siCtrl) or siRNA directed against ALKBH5 (siALKBH5) was determined by 2D TLC. We observed an approximately 30% increase of m^{6}A upon *ALKBH5* knockdown, indicating that ALKBH5 readily influences the levels of m^{6}A *in vivo* (representative images shown; *n* = 3 biological replicates; mean ± s.e.m.; unpaired Student's *t*-test, *$P \leq 0.05$). **d**, ALKBH5 expression decreases m^{6}A in HEK293T cells. The relative abundance of m^{6}A versus (A + C + U) in mRNA of HEK293T cells expressing GST vector (Ctrl) or ALKBH5 with an N-terminal GST tag (GST-ALKBH5) was determined by 2D TLC. We observed a significant decrease of m^{6}A upon ALKBH5 expression, indicating that SLKBH5 readily influences levels of m^{6}A *in vivo* (representative images shown; *n* = 3 biological replicates; mean ± s.e.m.; unpaired Student's *t*-test, **$P \leq 0.01$).

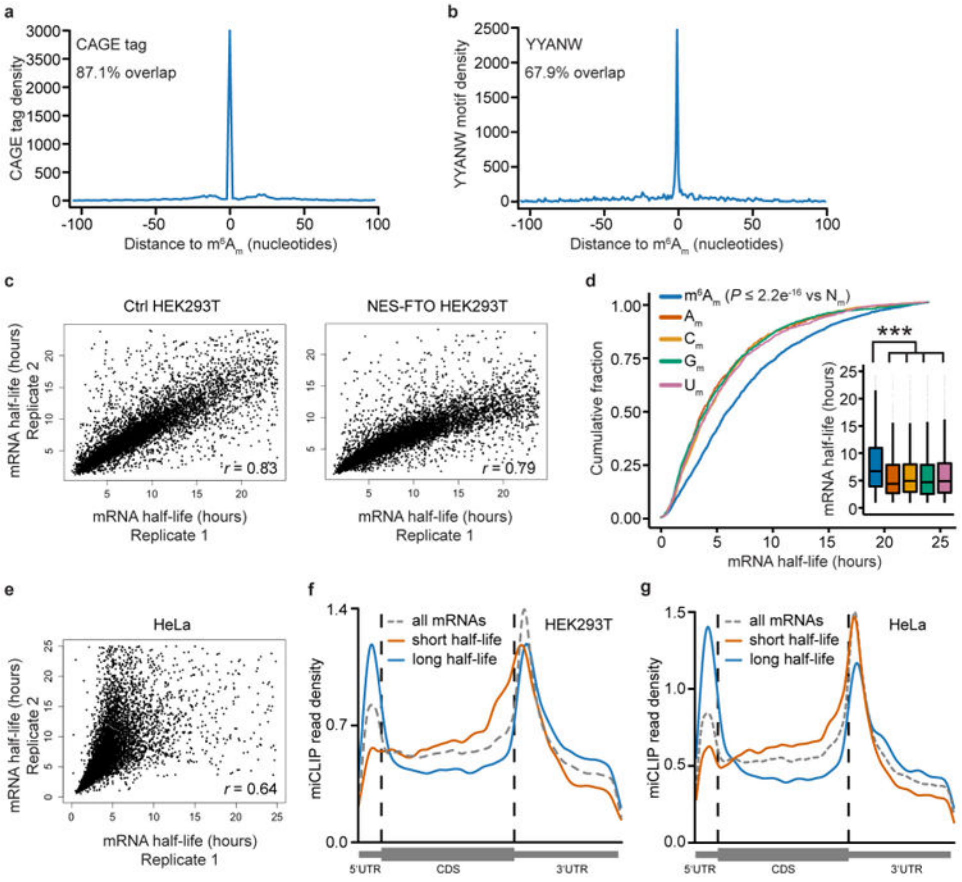

Extended Data Figure 5. Newly mapped m^{6}A$_m$ clusters overlap with transcription start sites (TSS) and the YYANW initiator core motif and mark mRNAs for increased half-life

a, **b**, To confirm that that the residues identified as m^{6}A$_m$ in miCLIP reflect transcription initiation sites, we searched for known TSS and transcription initiation sequences around each m^{6}A$_m$-containing region. Notably, owing to the calling algorithm, these regions do not contain any 5′ UTR m^{6}A. To identify genome-wide positions of the TSS we used published CAGE-seq datasets (see Methods). Shown is the nucleotide distance of the called m^{6}A$_m$ from TSS (**a**) and YYANW (**b**). These results demonstrate that TSS and the YYANW core initiator sequence are highly clustered at m^{6}A$_m$-containing regions (5′-most nucleotide is at position 0 on the *x*-axis). This suggests that the called m^6A_m-containing regions reflect true TSS. **c**, Related to Fig. 3a, c. Correlation of half-life replicates derived from Flag-transfected (Ctrl, left scatter plot) or Flag-NES-FTO-transfected (NES-FTO, right scatter plot) HEK293T cells. The Pearson correlation coefficient *(r)* is shown for each comparison and indicates high correlation between replicates. **d**, mRNA stability is determined by the modification state of the first encoded nucleotide in HeLa cells. Cumulative distribution plot of the half-life for mRNAs that start with m^6A_m, A_m, C_m, G_m and U_m. The half-life of mRNAs starting with an m^6A_m is approximately 2.5 h longer compared to mRNAs starting with A_m, C_m, G_m or U_m. Notably, for this analysis we used m^6A_m mRNAs identified in HEK293T cells to analyse published half-life data sets from HeLa cells[40]. This allowed us to determine if the stabilizing effect of m^6A_m on mRNA half-lives is conserved across different cell types. Indeed, the increase in m^6A_m mRNA half-life compared to other starting nucleotides was similar to what we observed in Fig. 3a (n = 2,401 (m^6A_m); 645 (A_m); 1,310 (C_m); 988 (G_m); 1,533 (U_m); data represents the average from two independent data sets; each box shows the first quartile, median, and third quartile; whiskers represent 1.5 × interquartile ranges; grey dots represent outliers; one-way ANOVA with Tukey's post hoc test, $^{***}P<2.2 \times 10^{-16}$ versus m^6A_m). **e**, related to Extended Data Fig. 6d, g. Correlation of half-life replicates derived from published HeLa cell datasets[40]. The Pearson correlation coefficient *(r)* is shown and indicates high correlation between replicates. **f**, Stable mRNAs show enrichment of m^6A_m miCLIP reads in HEK293T cells. miCLIP involves recovery of RNA fragments that interact with a 6mA-specific antibody, and thus recover m^6A- and m^6A_m-containing RNA fragments. The sequenced fragments, or miCLIP reads, map internally when they are m^6A. However, m^6A_m maps at the 5′ ends of transcripts. To determine whether mRNAs with long half-life show m^6A_m enrichment, we performed metagene analysis of HEK293T cell-derived miCLIP tag distribution in mRNAs that are in the top quartile of mRNA stability (blue) and the bottom quartile of mRNA stability (orange). The miCLIP tag distribution of all mRNAs is shown as a grey dashed line. On all mRNAs, miCLIP reads were enriched around the stop codon, a pattern that reflects the typical distribution of m^6A in mRNA. Additional enrichment of miCLIP reads was seen in the 5′ UTR, which we previously showed primarily reflects m^6A_m residues[12]. However, when we examined mRNAs with a long half-life (≥ 10 h), we observed a pronounced enrichment of miCLIP reads in the 5′ UTR. In contrast, mRNAs with a short half-life (≤3 h) exhibit markedly fewer miCLIP reads in the 5′ UTR. These data suggest that m^6A_m is associated with increased mRNA stability (*n* = 10,123 (all mRNAs); 820 (short half-life); 2,871 (long half-life)). **g**, Stable mRNAs show enrichment of m^6A_m miCLIP reads in HeLa cells. Similar to f, however, for this analysis we used miCLIP reads derived from HEK293T cells to analyse published half-life datasets from HeLa cells[40]. A marked enrichment of miCLIP reads was seen in the 5′ UTR of stable mRNAs, indicating elevated prevalence of m^6A_m in these mRNAs. These data suggest that m^6A_m is associated with increased mRNA stability, not only in HEK293T cells but also in HeLa cells. Importantly, the results are quantitatively similar to the results shown in **f**, indicating that m^6A_m mRNAs identified in HEK293T cells behave similarly in HeLa cells. (*n* = 18,286 (all mRNAs); 4,552 (short half-life); 3,619 (long half-life)).

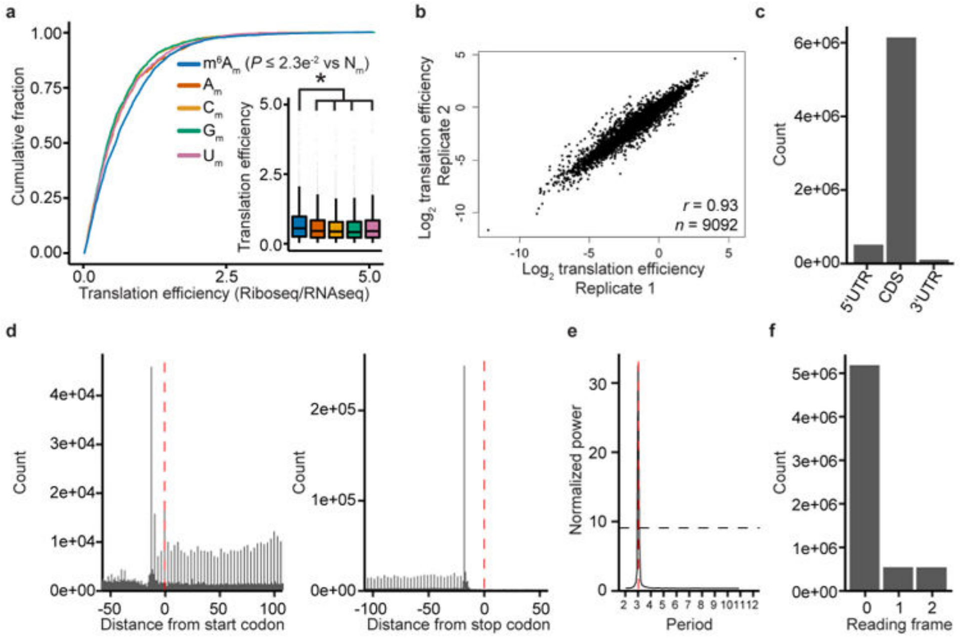

Extended Data Figure 6. m^6A_m mRNAs show increased translation efficiency

a, mRNA translation efficiency is associated with the modification state of the first encoded nucleotide in HEK293 cells. Cumulative distribution plot of the translation efficiency for mRNAs that start with m^6A_m, A_m, C_m, G_m and U_m. The translation efficiency of mRNAs starting with an m^6A_m is significantly higher compared to mRNAs starting wit h A_m, C_m, G_m or U_m (n = 3,024 (m^6A_m); 921 (A_m); 1,788 (C_m); 1,351 (G_m); 2,008 (U_m); data represent the average from two independent previously published ribosome profiling data sets[53]; each box shows the first quartile, median, and third quartile; whiskers represent 1.5 × interquartile ranges; grey dots represent outliers; one-way ANOVA with Tukey's post hoc test, $*P \leq 2.3 \times 10^{-2}$ versus m^6A_m). **b**, Correlation of translation efficiency replicates derived HEK293T cells. The Pearson correlation coefficient *(r)* is shown. **c**, Distribution of reads between the coding sequence (CDS) and UTRs. High coverage in the CDS compared to UTRs verifies ribosome-derived footprints. **d**, Total number of ribosome footprints near the start and stop codon of transcripts. **e**, Three-nucleotide periodicity demonstrates ribosome-derived footprints. **f**, Position of ribosome footprints relative to the reading frame.

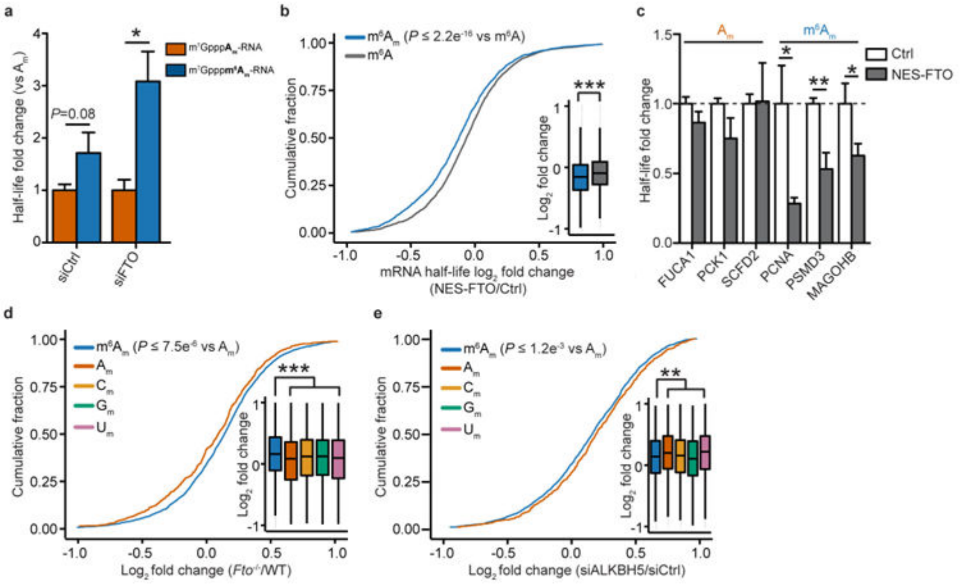

Extended Data Figure 7. Expression changes of m^6A_m, m^6A and A_m mRNAs upon NES-FTO expression and FTO or ALKBH5 deficiency

a, m^6A_m mRNAs exhibit increased half-life compared to A_m mRNAs *in vivo*.HEK293T cells were electroporated with *in vitro*-synthesized mRNAsstarting with either of two extended caps: m^7Gppp A_m or $m^7Gpppm^6A_m$.We then isolated cellular poly(A) RNA and determined the *in vivo* half-life of the electroporated A_m- and m^6A_m-containing mRNA by qRT-PCR.In control siRNA-treated HEK293T cells (siCtrl), the m^6A_m mRNAshowed a trend towards increased half-life compared to the A_m mRNA(unpaired Student's *t*-test, P = 0.08). Notably, when we performed the sameexperiment in FTO siRNA-treated cells (siFTO) to prevent demethylationof m^6A_m, the m^6A_m mRNA half-life was significantly increased (n = 3biological replicates; mean ± s.e.m.; unpaired Student's *t*-test, $P \leq 0.05$). **b**, NES-FTO expression preferentially affects the half-life of m^6A_m mRNAscompared to m^6A mRNAs. Changes in half-life of mRNAs containingeither m^6A_m or m^6A in HEK293T cells transfected with either Flag vector(Ctrl) or FTO with an N-terminal nuclear export signal (NES-FTO)were determined by RNA-seq. m^6A_m mRNAs are generally long-lived (see Fig. 3a) and show reduced half-lives after NES–FTO expression. We asked if FTO could elicit a similar effect on mRNAs containing m^6A. For this experiment, we used a set of mRNAs with annotated m^6A residues[12], excluding those which also contain an annotated m^6A_m. NES-FTO expression reduced the half-life of m^6A_m mRNAs but did not have any substantial effect on the half-life of m^6A mRNAs. These data support the idea that FTO preferentially targets m^6A_m compared to m^6A (n = 2,049 (m^6A_m); 2,495 (m^6A); data represent the average from two independent datasets; each box shows the first quartile, median, and third quartile; whiskers represent 1.5 × interquartile ranges; grey dots represent outliers; one-way ANOVA with Tukey's post hoc test, $***P \leq 2.2 \times 10^{-16}$ versus m^6A). **c**, NES-FTO expression preferentially affects the half-life of m^6A_m mRNAs compared to A_m mRNAs. Changes in half-life of A_m mRNAs (*FUCA1, PCK1, SCFD2*) and m^6A_m mRNAs *(PCNA, PSMD3, MAGOHB)* in HEK293T cells transfected with either Flag vector (Ctrl) or FTO with an N-terminal nuclear export signal (NES-FTO) were determined by BrU pulse-chase analysis and subsequent qRT-PCR. m^6A_m mRNAs show a significant reduction in half-life after

NES-FTO expression whereas the half-life of A_m mRNAs is less affected. These data examine specific mRNAs in contrast to the whole-transcriptome analysis presented in Fig. 3c and also demonstrate the stabilization effect of m^6A_m using a different method to measure mRNA half-life (that is, BrU pulse-chase labelling) other than transcriptional inhibition ($n = 3$ biological replicates; mean ± s.e.m.; unpaired Student's *t*-test, $^*P \leq 0.05$, $^{**}P \leq 0.01$). **d**, The expression of mRNAs containing either m^6A_m or A_m upon *Fto* knockout was determined by RNA-seq. *FTO* depletion ($Fto^{-/-}$) results in increased abundance of mRNAs with an annotated m^6A_m residue in liver tissue derived from *Fto*-knockout mice. Fold change was measured relative to the RNA levels measured in the same tissue obtained from wild-type littermates ($n = 2{,}048$ (m^6A_m); 1,025 (A_m); 2,081 (C_m); 1,742 (G_m); 1,242 (U_m); data represent the average from two independent data sets; each box shows the first quartile, median, and third quartile; whiskers represent 1.5 × interquartile ranges; grey dots represent outliers; one-way ANOVA with Tukey's post hoc test, $^{***}P \leq 7.5 \times 10^{-6}$ m^6A_m versus A_m and U_m). **e**, Knockdown of ALKBH5 does not increase the levels of m^6A_m mRNAs. The expression of mRNAs containing either m^6A_m or A_m upon *ALKBH5* knockdown in HEK293T cells was determined by RNA-seq. In contrast to knockdown or knockout of *FTO,* m^6A_m mRNAs are slightly less abundant than A_m mRNAs in *ALKBH5*-knockdown cells. This suggests that ALKBH5 does not target m^6A_m-containing mRNAs *in vivo* ($n = 3{,}111$ (m^6A_m); 1,928 (A_m); 4,382 (C_m); 3,110 (G_m); 3,998 (U_m); data represent the average from two independent datasets; each box shows the first quartile, median, and third quartile; whiskers represent 1.5 × interquartile ranges; grey dots represent outliers; one-way ANOVA with Tukey's post hoc test, $^{**}P \leq 1.2 \times 10^{-3}$ m^6A_m versus A_m and U_m).

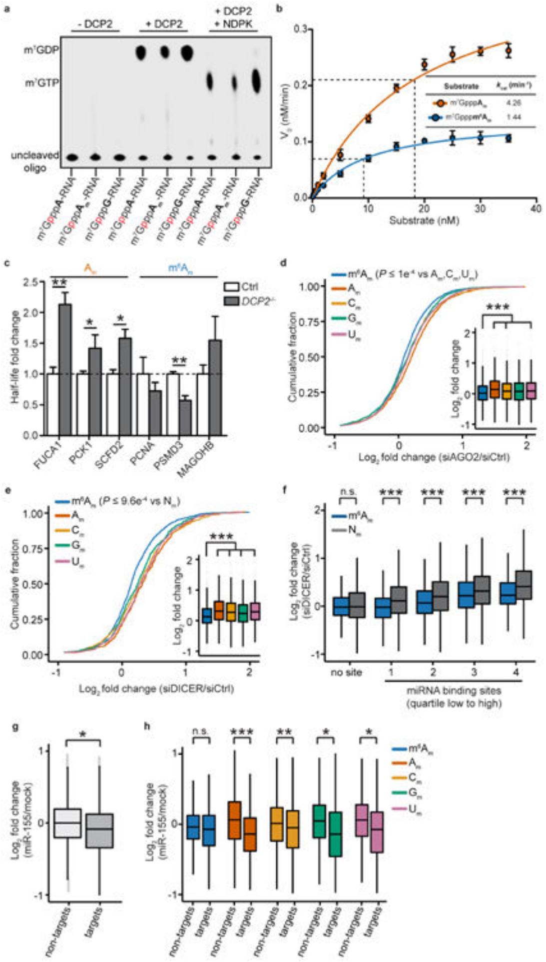

Extended Data Figure 8. m^6A_m mRNAs are resistant to DCP2-mediated decapping and microRNA-mediated gene silencing

a, DCP2 decapping products are m^7GDP. Here we confirm the identity of the putative m^7GDP decapping product in the decapping assay by treatment with nucleoside-diphosphate kinase (NDPK). The shift to the m^7GTP position confirms that the released product is m^7GDP. A cap-labelled RNA with a guanosine as the first nucleotide was used as a positive control (lanes 3, 6, 9; the red ‘p’ denotes the position of the ^{32}P). **b**, Michaelis-Menten curves of 10 nM DCP2 reacting with $m^7Gpppm^6A_m$ (blue) or m^7GpppA_m (orange) for 30 min at 37 °C. DCP2 shows higher decapping activity towards m^7GpppA_m than to $m^7Gpppm^6A_m$ (the dashed lines indicate the K_m on the × axis; $n = 3$ biological replicates; mean ± s.e.m.). **c**, DCP2 depletion preferentially stabilizes A_m mRNAs compared to m^6A_m mRNAs. Changes in half-life of A_m mRNAs (*FUCA1, PCK1, SCFD2*) and m^6A_m mRNAs *(PCNA, PSMD3, MAGOHB)* in HEK293T cells transfected with either Flag vector (Ctrl) or *DCP2*-knockout cells (*DCP2*$^{-/-}$) were determined by BrU pulse-chase analysis and subsequent qRT-PCR. A_m mRNAs show a significant increase in half-life after DCP2 depletion whereas the half-life of m^6A_m mRNAs was not significantly increased. These data are related to the whole-transcriptome expression analysis presented in Fig. 4c and indicate that, in addition to the observed abundance changes of non-m^6A_m mRNAs versus m^6A_m mRNAs, DCP2 also selectively affects the half-life of specifically examined mRNAs ($n = 3$

biological replicates; mean ± s.e.m.; unpaired Student's *t*-test, $*P \leq 0.05$, $**P \leq 0.01$). **d**, In Fig. 4d, we found that m^6A_m mRNAs show less upregulation upon *DICER* knockdown than mRNAs beginning with other nucleotides. We wanted to further examine this concept using additional independent datasets of gene expression following depletion of proteins required for microRNA-mediated mRNA degradation, such as members of the Argonaute protein family. Measurement of mRNA expression in *AGO2*-knockdown HEK293T cells (siAGO2) compared to control cells (siCtrl)[21] revealed more pronounced upregulation of non-m^6A_m mRNAs compared to those that have m^6A_m ($n =$ 2,080 (m^6A_m); 596 (A_m); 1,085 (C_m); 805 (G_m); 1,274 (U_m); data represent the average from two independent datasets; each box shows the first quartile, median, and third quartile; whiskers represent 1.5 × interquartile ranges; grey dots represent outliers; one-way ANOVA with Tukey's post hoc test, $***P \leq 1 \times 10^{-4}$ m^6A_m versus A_m, C_m and U_m). **e**, Similar to Fig. 4d, but here we only look at the expression changes of mRNAs that contain TargetScan-predicted microRNA-binding sites. Applying this filter criteria, we also observed that *DICER* knockdown in HEK293T cells (siDICER)[21] resulted in more pronounced upregulation of non-m^6A_m miRNA target mRNAs compared to those that have m^6A_m ($n =$ 1,208 (m^6A_m); 359 (A_m); 607 (C_m); 467 (G_m); 713 (U_m); data represent the average from two independent datasets; each box shows the first quartile, median, and third quartile; whiskers represent 1.5 × interquartile ranges; grey dots represent outliers; one-way ANOVA with Tukey's post hoc test, $***P \leq 9.6 \times 10^{-4}$ versus $m^6A_mN_m$, where $N_m = A_m$, C_m, G_m or U_m). **f**, In Fig. 4d and Extended Data Fig. 8e we show that m^6A_m mRNAs exhibit less upregulation upon *DICER* knockdown than mRNAs beginning with other nucleotides. We wanted to examine this concept further using additional filtering criteria. Thus, we asked if m^6A_m mRNA resistance to DICER depletion is dependent on the number of microRNA-binding sites. Therefore, we divided mRNAs into five groups: mRNAs that do not contain a predicted microRNA-binding site (0) and mRNAs that belong to specific quartiles that we assigned depending on the number of microRNA-binding sites (low (1) to high (4)). Notably, we did not observe any expression difference between m^6A_m mRNAs and non-m^6A_m mRNAs that do not carry predicted microRNA-binding sites. However, there was a clear increase in mRNA expression for mRNAs that contain microRNA-binding sites, and this increase was dependent on the number of microRNA-binding sites. Notably, for each quartile, m^6A_m mRNAs were significantly less upregulated than N_m mRNAs (n = 91 versus 89 (m^6A_m versus N_m; 1), 252 versus 339 (m^6A_m versus N_m; 1), 311 versus 454 (m^6A_m versus N_m; 2), 247 versus 541 (m^6A_m versus N_m; 3), 229 versus 512 (m^6A_m versus N_m; 4); data represent the average from two independent datasets; number of microRNA-binding sites in each quartile: 1 = 1–3; 2 = 4-6; 3 = 7–12; 4 = 13-54; each box shows the first quartile, median, and third quartile; whiskers represent 1.5 × interquartile ranges; one-way ANOVA with Tukey's post hoc test, $*P \leq 0.05$, $***P \leq 0.001$, n.s., not significant). **g**, In Fig. 4d and Extended Data Fig. 9d-f we show that m^6A_m mRNAs are largely resistant to expression changes upon global inhibition of the microRNA machinery. We next asked whether introduction of a single microRNA also leads to differential responses of m^6A_m mRNAs compared to non-m^6A_m mRNAs. We used a published dataset where HeLa cells were transfected with a miR-155 duplex to achieve microRNA-specific mRNA degradation[22]. For this analysis, we used m^6A_m mRNAs mapped in HEK293T cells. We first asked if we could observe a differential effect of mRNA degradation on miR-155 target[52] and non-target mRNAs in the HeLa cell dataset. Indeed, miR-155 target mRNAs were significantly more suppressed in miR-155-transfected HeLa cells. This confirms that miR-155 target mRNA degradation can be detected in this dataset ($n = 1{,}131$ (target); 7,700 (non-target; data represent the average from two independent datasets; each box shows the first quartile, median, and third quartile; whiskers represent 1.5 × interquartile ranges; grey dots represent outliers; one-way ANOVA with Tukey's post hoc test, $**P \leq 2.2 \times 10^{-16}$). **h**, m^6A_m mRNAs show resistance to miR-155-mediated mRNA degradation. We tested if the identity of the first nucleotide affects the response of miR-155 target mRNAs to miR-155-mediated mRNA degradation. We observed that miR-155 target mRNAs that start with m^6A_m show no significant suppression upon miR-155 transfection compared to non-target mRNAs that start with m^6A_m. However, expression of miR-155 target mRNAs that start with A_m, C_m, G_m or U_m was significantly suppressed compared to non-target mRNAs that start with A_m, C_m, G_m or U_m. These data suggest that the presence m^6A_m can reduce the silencing efficiency of a single microRNA *in vivo (*$n = 1{,}714$ versus 232 (m^6A_m, non-target versus target); 953 versus 158 (A_m, non-target versus target); 1,848 versus 281 (C_m, non-target versus target); 1,394 versus 182 (G_m); 1,809 versus 278 (U_m, non-target versus target); each box shows the first quartile, median, and third quartile; whiskers represent 1.5 × interquartile ranges; one-way ANOVA with Tukey's post hoc test, $*P \leq 0.05$ non-target versus miR-155 target, $**P \leq 0.01$ non-target versus miR-155 target, $***P \leq 0.001$ non-target versus miR-155 target).

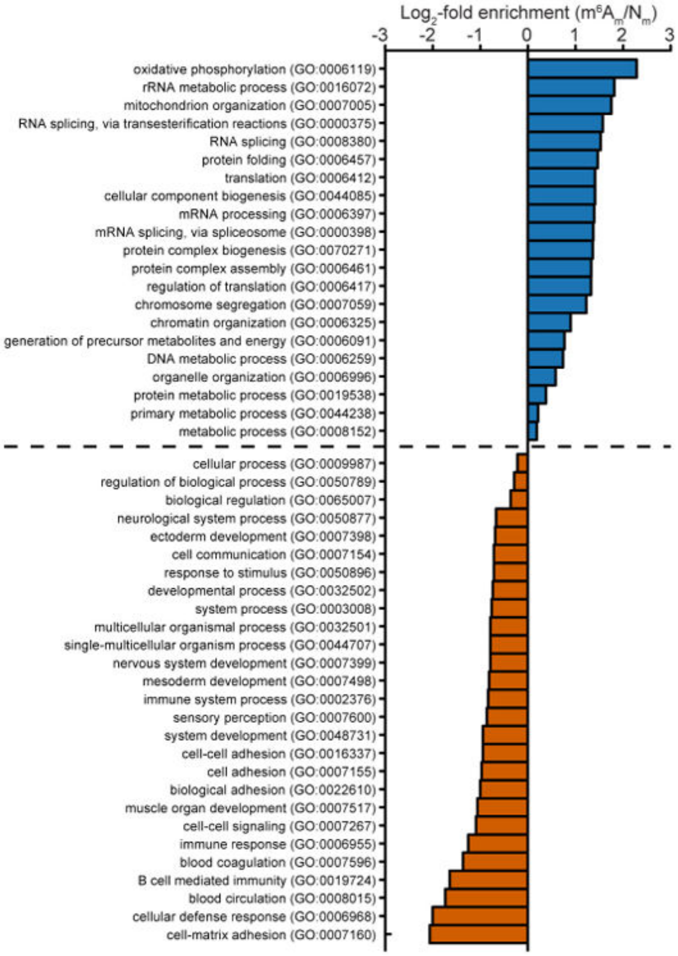

Extended Data Figure 9. m^{6}A$_m$-containing mRNAs are enriched for oxidative phosphorylation, metabolic pathways, and components of the RNA processing machinery

Gene Ontology (GO) analysis of m^{6}A$_m$ mRNAs. We used PANTHER overrepresentation test and Bonferroni correction with a *P* value threshold of <0.01. All annotated non-m^{6}A$_m$-containing mRNAs (*N*$_m$) were used as the background gene list. m^{6}A$_m$ mRNAs are overrepresented in cellular pathways associated with oxidative phosphorylation and metabolism as well as mRNA processing and translation, suggesting that m^{6}A$_m$ controls cellular pathways by stabilizing specific populations of mRNAs.

Extended Data Table 1

Tables of kinetic parameters for FTO and other enzymes from the family of Fe(II) and α-ketoglutarate-dependent oxygenases

a

Enzyme	Substrate	K_m (μM)	k_{cat}(min^{-1})	k_{cat}/K_m(min^{-1} μM^{-1})	Species	PMID
AlkB	CA(m3C)AT	0.29	23	78.3	*E.Coli*	19706517
FTO	m7Gppp(m6Am)CA	1.34	8.78	6.552	Human	current study

a

Enzyme	**Substrate**	**K_m (μM)**	**k_{cat}(min^{-1})**	**k_{cat}/K_m(min^{-1} μM^{-1})**	**Species**	**PMID**
AlkB	CA(m1A)AT	0.06	5.4	97.0	*E.Coli*	19706517
JmjC	H3K9me3	3.3	2.71	0.8212	Human	26645689
PHD2	aKG	0.9	2.3	2.555	Human	25857330
KDM4C	H3K4me3K9me3	1.2	0.45	0.375	Human	26747609
FTO	CA(m6A)CA	0.409	0.296	0.724	Human	22002720
ALKBH5	CA(m6A)CA	1.38	0.169	0.122	Human	23177736

b

Enzyme	**Substrate**	**K_m (μM)**	**k_{cat}(min^{-1})**	**k_{cat}/K_m**(min^{-1} μM^{-1})	**Species**	**PMID**
FTO	m7Gppp(m6Am)CA	1.34	8.78	6.552	Human	current study
	m7Gppp(m6A)CA	16.09	7.77	0.483	Human	current study
	GG(m6A)CU	9.29	0.54	0.058	Human	current study
	m7GpppAC(m6A)	6.4	0.46	0.071	Human	current study

a, Shown are published kinetic parameters for different enzymes and their respective substrates. PMID, Pubmed identifier.

b, Shown are kinetic parameters collected for FTO in the current study.

Supplementary Material

Refer to Web version on PubMed Central for supplementary material.

Acknowledgments

We thank P. Holliger for assistance with TGK-polymerase, A. O. Olarerin-George for assistance with data analysis, K. Meyer for early contributions on FTO-target mapping, and members of the Jaffrey laboratory for helpful comments and suggestions. This work was supported by NIH grants R01DA037755 (S.R.J.), P01HD67244 and R37HL87062 (S.S.G.), T32HD060600 and a Clinical and Translational Science Center Fellowship (A.V.G.), T32CA062948 (B.F.P.), and R01GM067005 (M.K.), by the French Centre National de la Recherche Scientifique (F.D.) and by the DFG (J.M. and B.L.).

References

1. Meyer KD, et al. Comprehensive analysis of mRNA methylation reveals enrichment in 3′ UTRs and near stop codons. Cell. 2012; 149:1635–1646. [PubMed: 22608085]
2. Dominissini D, et al. Topology of the human and mouse m6A RNA methylomes revealed by m6A-seq. Nature. 2012; 485:201–206. [PubMed: 22575960]
3. Zheng G, et al. ALKBH5 is a mammalian RNA demethylase that impacts RNA metabolism and mouse fertility. Mol Cell. 2013; 49:18–29. [PubMed: 23177736]
4. Jia G, et al. N6-methyladenosine in nuclear RNA is a major substrate of the obesity-associated FTO. Nat Chem Biol. 2011; 7:885–887. [PubMed: 22002720]
5. Adams JM, Cory S. Modifed nucleosides and bizarre 5′-termini in mouse myeloma mRNA. Nature. 1975; 255:28–33. [PubMed: 1128665]
6. Wei CM, Gershowitz A, Moss B. Methylated nucleotides block 5′ terminus of HeLa cell messenger RNA. Cell. 1975; 4:379–386. [PubMed: 164293]
7. Dafs S, et al. 2′-O methylation of the viral mRNA cap evades host restriction by IFIT family members. Nature. 2010; 468:452–456. [PubMed: 21085181]

8. Wei C, Gershowitz A, Moss B. N6, O2′-dimethyladenosine a novel methylated ribonucleoside next to the 5′ terminal of animal cell and virus mRNAs. Nature. 1975; 257:251–253. [PubMed: 1161029]
9. Keith JM, Ensinger MJ, Moss B. HeLa cell RNA (2′-O-methyladenosine-N6-)-methyltransferase specifc for the capped 5′-end of messenger RNA. J Biol Chem. 1978; 253:5033–5039. [PubMed: 670176]
10. Wei CM, Gershowitz A, Moss B. 5′-Terminal and internal methylated nucleotide sequences in HeLa cell mRNA. Biochemistry. 1976; 15:397–401. [PubMed: 174715]
11. Hess ME, et al. The fat mass and obesity associated gene (Fto) regulates activity of the dopaminergic midbrain circuitry. Nat Neurosci. 2013; 16:1042–1048. [PubMed: 23817550]
12. Linder B, et al. Single-nucleotide-resolution mapping of m6A and m6Am throughout the transcriptome. Nat Methods. 2015; 12:767–772. [PubMed: 26121403]
13. Fu Y, et al. FTO-mediated formation of N6-hydroxymethyladenosine and N6-formyladenosine in mammalian RNA. Nat Commun. 2013; 4:1798. [PubMed: 23653210]
14. Kruse S, et al. A novel synthesis and detection method for cap-associated adenosine modifcations in mouse mRNA. Sci Rep. 2011; 1:126. [PubMed: 22355643]
15. Vujovic P, et al. Fasting induced cytoplasmic Fto expression in some neurons of rat hypothalamus. PLoS One. 2013; 8:e63694. [PubMed: 23671692]
16. Forrest AR, et al. A promoter-level mammalian expression atlas. Nature. 2014; 507:462–470. [PubMed: 24670764]
17. Schwartz S, et al. Perturbation of m6A writers reveals two distinct classes of mRNA methylation at internal and 5′ sites. Cell Reports. 2014; 8:284–296. [PubMed: 24981863]
18. Wang Z, et al. The hDcp2 protein is a mammalian mRNA decapping enzyme. Proc Natl Acad Sci USA. 2002; 99:12663–12668. [PubMed: 12218187]
19. Wu L, Belasco JG. Let me count the ways: mechanisms of gene regulation by miRNAs and siRNAs. Mol Cell. 2008; 29:1–7. [PubMed: 18206964]
20. Rehwinkel J, Behm-Ansmant I, Gatfeld D, Izaurralde E. A crucial role for GW182 and the DCP1:DCP2 decapping complex in miRNA-mediated gene silencing. RNA. 2005; 11:1640–1647. [PubMed: 16177138]
21. Schmitter D, et al. Efects of Dicer and Argonaute down-regulation on mRNA levels in human HEK293 cells. Nucleic Acids Res. 2006; 34:4801–4815. [PubMed: 16971455]
22. Guo H, Ingolia NT, Weissman JS, Bartel DP. Mammalian microRNAs predominantly act to decrease target mRNA levels. Nature. 2010; 466:835–840. [PubMed: 20703300]
23. Meyer KD, et al. 5′ UTR m6A promotes cap-independent translation. Cell. 2015; 163:999–1010. [PubMed: 26593424]
24. Liu L, et al. Decomposition of RNA methylome reveals co-methylation patterns induced by latent enzymatic regulators of the epitranscriptome. Mol Biosyst. 2015; 11:262–274. [PubMed: 25370990]
25. Zhou J, et al. Dynamic m6A mRNA methylation directs translational control of heat shock response. Nature. 2015; 526:591–594. [PubMed: 26458103]
26. Zhao X, et al. FTO-dependent demethylation of N6-methyladenosine regulates mRNA splicing and is required for adipogenesis. Cell Res. 2014; 24:1403–1419. [PubMed: 25412662]
27. Fischer J, et al. Inactivation of the Fto gene protects from obesity. Nature. 2009; 458:894–898. [PubMed: 19234441]
28. Boissel S, et al. Loss-of-function mutation in the dioxygenase-encoding FTO gene causes severe growth retardation and multiple malformations. Am J Hum Genet. 2009; 85:106–111. [PubMed: 19559399]
29. Jonas S, Izaurralde E. Towards a molecular understanding of microRNA-mediated gene silencing. Nat Rev Genet. 2015; 16:421–433. [PubMed: 26077373]
30. Sommer S, Lavi U, Darnell JE Jr. The absolute frequency of labeled N-6-methyladenosine in HeLa cell messenger RNA decreases with label time. J Mol Biol. 1978; 124:487–499. [PubMed: 712844]

31. Debart, F., Lavergne, T., Janin, M., Dupouy, C., Vasseur, JJ. Current Protocols in Nucleic Acid Chemistry. Beaucage, S., et al., editors. Vol. 43. John Wiley & Sons, Inc.; 2010. p. 3.19.11-3.19.27.
32. Lavergne T, Bertrand JR, Vasseur JJ, Debart F. A base-labile group for 2′-OH protection of ribonucleosides: a major challenge for RNA synthesis. Chemistry. 2008; 14:9135–9138. [PubMed: 18767078]
33. Zlatev I, et al. Chemical solid-phase synthesis of 5′-triphosphates of DNA, RNA, and their analogues. Org Lett. 2010; 12:2190–2193. [PubMed: 20420425]
34. Thillier Y, et al. Synthesis of 5′ cap-0 and cap-1 RNAs using solid-phase chemistry coupled with enzymatic methylation by human (guanine-N7)-methyl transferase. RNA. 2012; 18:856–868. [PubMed: 22334760]
35. Paesen GC, et al. X-ray structure and activities of an essentia Mononegavirales L-protein domain. Nat Commun. 2015; 6:8749. [PubMed: 26549102]
36. Barral K, et al. Development of specific dengue virus 2′-O- and N7-methyltransferase assays for antiviral drug screening. Antiviral Res. 2013; 99:292–300. [PubMed: 23769894]
37. Wang Z, Jiao X, Carr-Schmid A, Kiledjian M. The hDcp2 protein is a mammalian mRNA decapping enzyme. Proc Natl Acad Sci USA. 2002; 99:12663–12668. [PubMed: 12218187]
38. Liu SW, Jiao X, Welch S, Kiledjian M. Analysis of mRNA decapping. Methods Enzymol. 2008; 448:3–21. [PubMed: 19111168]
39. Cozens C, Pinheiro VB, Vaisman A, Woodgate R, Holliger P. A short adaptive path from DNA to RNA polymerases. Proc Natl Acad Sci USA. 2012; 109:8067–8072. [PubMed: 22566643]
40. Wang X, et al. N6-methyladenosine-dependent regulation of messenger RNA stability. Nature. 2014; 505:117–120. [PubMed: 24284625]
41. Geula S, et al. Stem cells. m6A mRNA methylation facilitates resolution of naive pluripotency toward diferentiation. Science. 2015; 347:1002–1006. [PubMed: 25569111]
42. Dobin A, et al. STAR: ultrafast universal RNA-seq aligner. Bioinformatics. 2013; 29:15–21. [PubMed: 23104886]
43. Love MI, Huber W, Anders S. Moderated estimation of fold change and dispersion for RNA-seq data with DESeq2. Genome Biol. 2014; 15:550. [PubMed: 25516281]
44. Imamachi N, et al. BRIC-seq: a genome-wide approach for determining RNA stability in mammalian cells. Methods. 2014; 67:55–63. [PubMed: 23872059]
45. Moore MJ, et al. Mapping Argonaute and conventional RNA-binding protein interactions with RNA at single-nucleotide resolution using HITS-CLIP and CIMS analysis. Nat Protocols. 2014; 9:263–293. [PubMed: 24407355]
46. Xi H, et al. Analysis of overrepresented motifs in human core promoters reveals dual regulatory roles of YY1. Genome Res. 2007; 17:798–806. [PubMed: 17567998]
47. Dominissini D, et al. The dynamic N1-methyladenosine methylome in eukaryotic messenger RNA. Nature. 2016; 530:441–446. [PubMed: 26863196]
48. Smedley D, et al. The BioMart community portal: an innovative alternative to large, centralized data repositories. Nucleic Acids Res. 2015; 43(W1):W589–W598. [PubMed: 25897122]
49. Heyer EE, Ozadam H, Ricci EP, Cenik C, Moore MJ. An optimized kit-free method for making strand-specific deep sequencing libraries from RNA fragments. Nucleic Acids Res. 2015; 43:e2. [PubMed: 25505164]
50. Li B, Dewey CN. RSEM: accurate transcript quantification from RNA-Seq data with or without a reference genome. BMC Bioinformatics. 2011; 12:323. [PubMed: 21816040]
51. Grimson A, et al. MicroRNA targeting specificity in mammals: determinants beyond seed pairing. Mol Cell. 2007; 27:91–105. [PubMed: 17612493]
52. Yang JH, et al. starBase: a database for exploring microRNA-mRNA interaction maps from Argonaute CLIP-Seq and Degradome-Seq data. Nucleic Acids Res. 2011; 39:D202–D209. [PubMed: 21037263]
53. Iwasaki S, Floor SN, Ingolia NT. Rocaglates convert DEAD-box protein eIF4A into a sequence-selective translational repressor. Nature. 2016; 534:558–561. [PubMed: 27309803]

54. Ingolia NT, Brar GA, Rouskin S, McGeachy AM, Weissman JS. The ribosome profling strategy for monitoring translation in vivo by deep sequencing of ribosome-protected mRNA fragments. Nat Protocols. 2012; 7:1534–1550. [PubMed: 22836135]
55. Fallmann J, Sedlyarov V, Tanzer A, Kovarik P, Hofacker IL. AREsite2: an enhanced database for the comprehensive investigation of AU/GU/U-rich elements. Nucleic Acids Res. 2016; 44(D1):D90–D95. [PubMed: 26602692]
56. Friedman RC, Farh KK, Burge CB, Bartel DP. Most mammalian mRNAs are conserved targets of microRNAs. Genome Res. 2009; 19:92–105. [PubMed: 18955434]
57. Lorenz R, et al. ViennaRNA Package 2.0. Algorithms Mol Biol. 2011; 6:26. [PubMed: 22115189]
58. Huppert JL, Bugaut A, Kumari S, Balasubramanian S. G-quadruplexes: the beginning and end of UTRs. Nucleic Acids Res. 2008; 36:6260–6268. [PubMed: 18832370]
59. Beaudoin JD, Perreault JP. 5′-UTR G-quadruplex structures acting as translational repressors. Nucleic Acids Res. 2010; 38:7022–7036. [PubMed: 20571090]
60. Xu C, et al. Structures of human ALKBH5 demethylase reveal a unique binding mode for specific single-stranded N6-methyladenosine RNA demethylation. J Biol Chem. 2014; 289:17299–17311. [PubMed: 24778178]
61. Zhong S, et al. MTA is an Arabidopsis messenger RNA adenosine methylase and interacts with a homolog of a sex-specific splicing factor. Plant Cell. 2008; 20:1278–1288. [PubMed: 18505803]

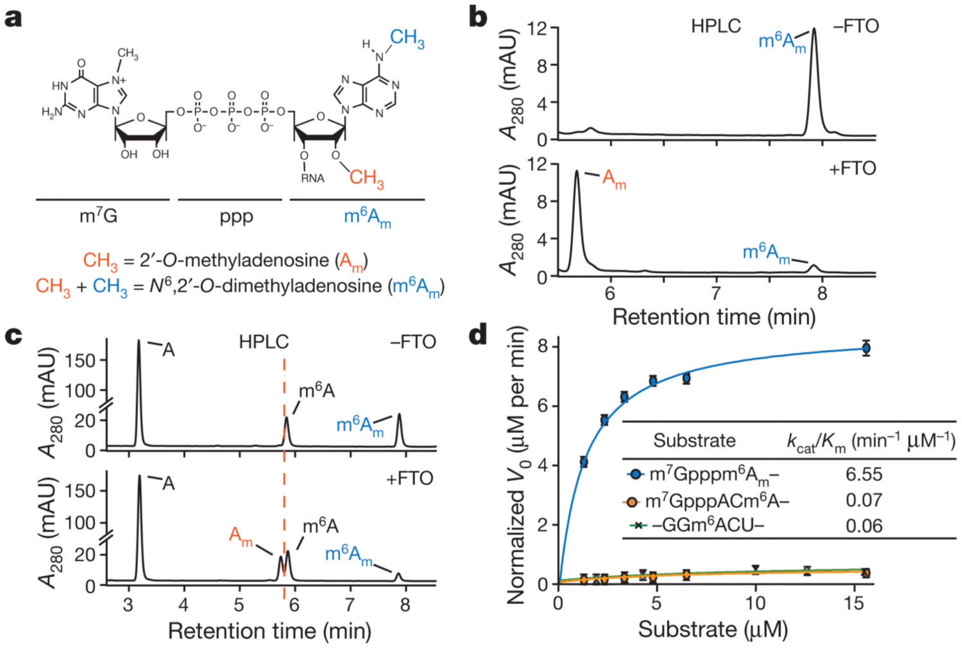

Figure 1. FTO prefers m^6A_m to m^6A as a substrate

a , Modifications of the extended mRNA cap. The first nucleotide (here shown as adenosine) adjacent to the m^7G and the 5′-to-5′ triphosphate (ppp) linker is subjected to 2′-*O*-methylation (orange) on the ribose, forming cap1. Cap1 can be further 2′-*O*-methylated at the second nucleotide to form cap2 (not depicted). 2′-*O*-methyladenosine (A_m) can be further converted to cap1m by N^6-methylation (blue), which results in N^6,*2′-O*-dimethyladenosine (m^6A_m). **b**, FTO efficiently converts m^6A_m to A_m. A synthetic oligonucleotide with a 5′-$m^7Gpppm^6A_m$ (2 μM) was incubated with FTO (100 nM FTO, 1 h), which readily converted m^6A_m to A_m (representative high-performance liquid chromatography (HPLC) track of $n = 3$ biological replicates). mAU, milli absorbance units. **c**, FTO preferentially demethylates m^6A_m compared to m^6A. An oligonucleotide with a 5′-$m^7Gpppm^6A_m$ cap was mixed in an equimolar ratio with an oligonucleotide containing internal m^6A. FTO (100 nM, 1 h) almost completely converted m^6A_m to A_m. Demethylation of m^6A was not detectable (representative HPLC track of $n = 3$ biological replicates). **d**, Michaelis-Menten kinetics of FTO for m^6A_m and m^6A. Owing to the increased activity of FTO with m^6A_m compared to m^6A, enzyme concentration was tenfold lower for m^6A_m (20 nM FTO for m^6A_m, 200 nM FTO for m^6A). The data was normalized to enzyme concentration ($m^7Gpppm^6A_m$ (blue), $m^7GpppACm^6A$ (orange), internal m^6A (green); $n = 3$ biological replicates; mean ± s.e.m; V_0 = initial reaction velocity).

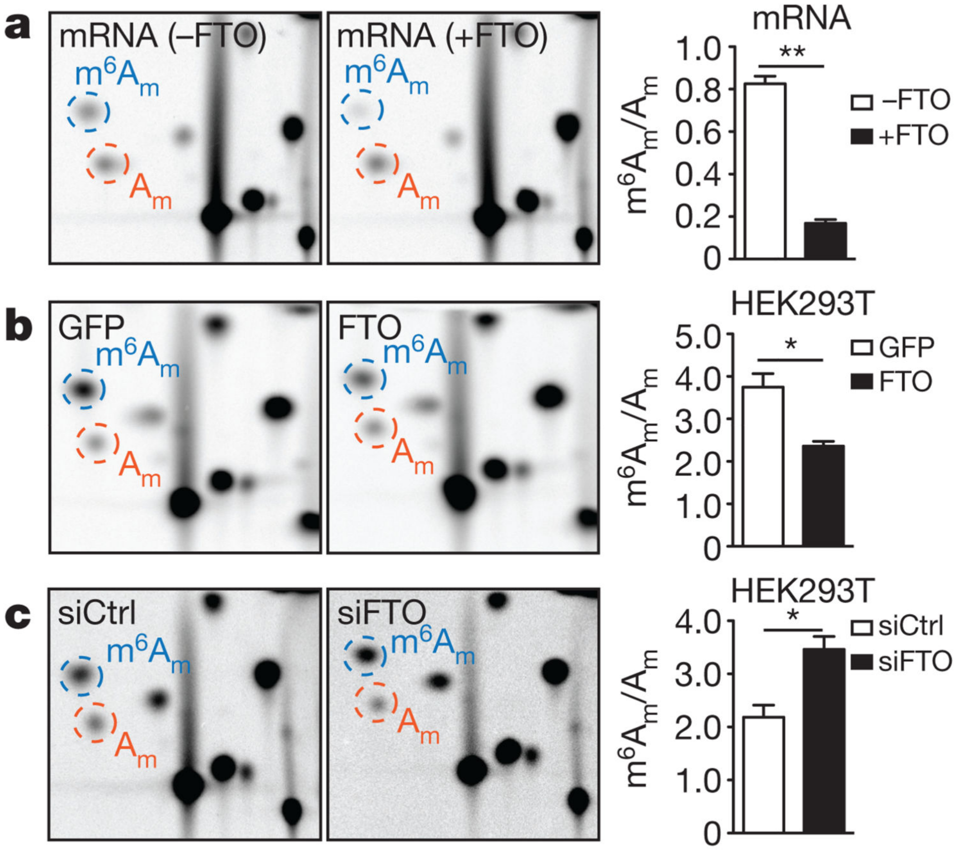

Figure 2. m^6A_m is the preferred substrate of FTO *in vivo*

a, FTO readily demethylates m^6A_m in mRNA. Relative abundance of modified adenosines in mRNA caps derived from mRNA treated with FTO (1 µM, 1 h; representative images shown; $n = 3$ biological replicates; mean ± s.e.m.; unpaired Student's *t*-test, $**P\leq$; 0.001). **b**, FTO expression decreases m^6A_m in HEK293T cells. Relative abundance of modified adenosines in mRNA caps of HEK293T cells expressing GFP (Flag-GFP) or wild-type FTO (Flag-FTO) (representative images shown; $n = 3$ biological replicates; mean ± s.e.m.; unpaired Student's *t*-test, $*P \leq 0.05$). **c**, *FTO* knockdown increases m^6A_m in HEK293T cells. Relative abundance of modified adenosines in mRNA caps of HEK293T cells transfected with scrambled siRNA (siCtrl) or siRNA directed against FTO (siFTO) (representative images shown; $n = 3$ biological replicates; mean ± s.e.m.; unpaired Student's *t*-test, $*P\leq$ 0.05).

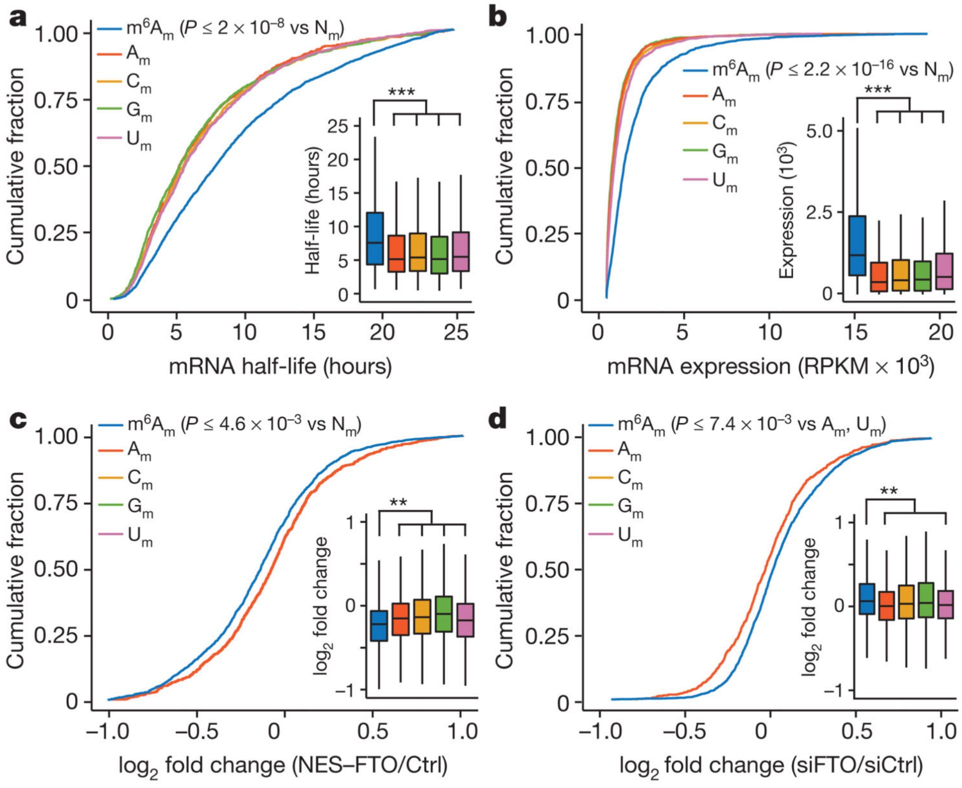

Figure 3. The presence of m^6A_m is associated with increased mRNA half-life

a , mRNA stability is determined by the first encoded nucleotide in HEK293T cells. Cumulative distribution plot of the half-life for mRNAs that start with m^6A_m, A_m, C_m, G_m and U_m (*n* = 2,515 (m^6A_m); 762 (A_m); 1,442 (C_m); 1,119 (G_m); 1,486 (U_m); data represent the average from two independent datasets; each box shows the first quartile, median, and third quartile; whiskers represent 1.5 × interquartile ranges; one-way ANOVA with Tukey's post hoc test, ***$P \leq 2 \times 10^{-8}$ versus m^6A_m; N_m = A_m, C_m, G_m or U_m). **b**, mRNA expression level is influenced by the modification state of the first encoded nucleotide in HEK293T cells. Cumulative distribution plot of the expression for mRNAs that start with m^6A_m, A_m, C_m, G_m and U_m (*n* = 2,536 (m^6A_m); 1,063 (A_m); 2,098 (C_m); 1,577 (G_m); 2,071 (U_m); data represent the average from two independent datasets; each box shows the first quartile, median, and third quartile; whiskers represent 1.5 × interquartile ranges; one-way ANOVA with Tukey's post hoc test, ***$P \leq 2.2 \times 10^{-16}$ versus m^6A_m). **c**, FTO expression leads to a global decrease of m^6A_m mRNA half-life in HEK293T cells. Changes in half-life of mRNAs containing either m^6A_m or A_m in cells transfected with either Flag vector (Ctrl) or FTO with an N-terminal nuclear export signal (NES-FTO) (*n* = 2,049 (m^6A_m); 951 (A_m); 1,442 (C_m); 1,119 (G_m); 1,486 (U_m); data represent the average from two independent datasets; each box shows the first quartile, median, and third quartile; whiskers represent 1.5 × interquartile ranges; one-way ANOVA with Tukey's post hoc test, **$P \leq 4.6 \times 10^{-3}$ versus m^6A_m). **d**, *FTO* knockdown leads to a global increase of m^6A_m mRNAs in HEK293T cells. Expression of mRNAs containing either m^6A_m or A_m upon *FTO* knockdown (*n* = 3,410 (m^6A_m); 1,355 (A_m); 2,636 (C_m); 1,994 (G_m); 2,558 (U_m); data represent the average from two independent mRNA expression datasets; each box shows the first quartile, median, and third quartile; whiskers represent 1.5 × interquartile ranges; one-way ANOVA with Tukey's post hoc test $^{**}P \leq 7.4 \times ^{-3}$ m^6A_m versus A_m and U_m).

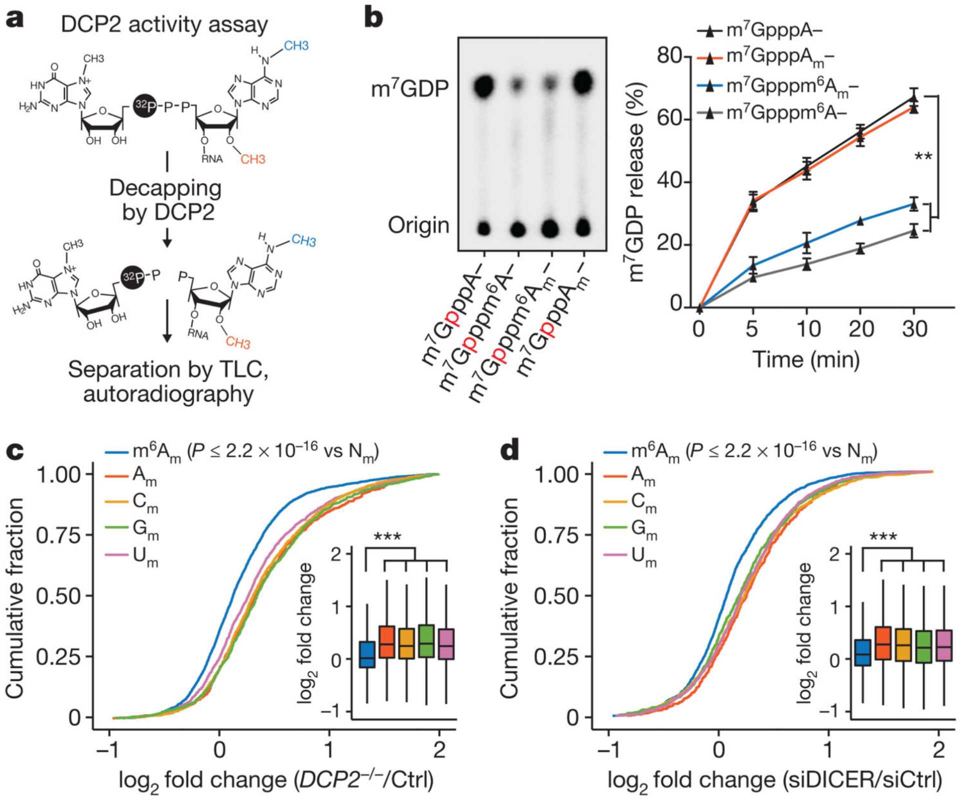

Figure 4. m^6A_m mRNAs are resistant to DCP2-mediated decapping

a, Schematic representation of the DCP2 *in vitro* decapping assay. The 5′ end of oligonucleotides containing the indicated form of adenosine (A, A_m, m^6A or m^6A_m) was enzymatically capped with [α-^{32}P]-m^{7}GTP. DCP2 causes the release of [α-^{32}P]-m^{7}GDP, which is detected by TLC. **b**, N^6-methylation of the cap-adjacent adenosine inhibits mRNA decapping *in vitro*. The presence of a 2′-*O*-methyl did not affect DCP2 activity relative to adenosine. However, addition of an N^6-methyl group decreased decapping efficiency ($n = 3$ biological replicates; mean ± s.e.m.; two-way ANOVA with Tukey's post hoc test, $**P \leq 0.01$). **c**, DCP2 deficiency primarily increases expression of non-m^6A_m mRNAs in the HEK293T cell transcriptome. Cumulative distribution plot of the expression of mRNAs that start with m^6A_m, A_m, C_m, G_m and U_m ($n =$ 3,287 (m^6A_m); 2,350 (A_m); 3,963 (C_m); 3,540 (G_m); 3,496 (U_m); data represent the average from two independent datasets; each box shows the first quartile, median, and third quartile; whiskers represent 1.5 × interquartile ranges; one-way ANOVA with Tukey's post hoc test, $**P \leq 2.2 \times 10^{-16}$ versus m^6A_m). **d**, m^6A_m reduces mRNA susceptibility to microRNA-mediated degradation. Cumulative distribution plot of the expression of mRNAs that start with m^6A_m, A_m, C_m, G_m or U_m ($n =$ 2,090 (m^6A_m); 623 (A_m); 1,109 (C_m); 852 (G_m); 1,322 (U_m); data represent the average from two independent datasets; each box shows the first quartile, median, and third quartile; whiskers represent 1.5 × interquartile ranges; one-way ANOVA with Tukey's post hoc test, $**P \leq 2.2 \times 10^{-16}$ versus m^6A_m).